COMMUNICATIONS IN COMPUTATIONAL PHYSICS
Vol. **2**, No. 5, pp. 900-932

Commun. Comput. Phys.
October 2007

The Lid-Driven Square Cavity Flow: From Stationary to Time Periodic and Chaotic

Salvador Garcia*

Departamento de Ciencias Matemáticas y Físicas,
Universidad Católica de Temuco, Casilla 15-D Temuco, Chile.

Received 12 September 2006; Accepted (in revised version) 14 December 2006

Communicated by Roger Temam

Available online 20 March 2007

Abstract. Ranging from Re=100 to Re=20,000, several computational experiments are conducted, Re being the Reynolds number. The primary vortex stays put, and the long-term dynamic behavior of the small vortices determines the nature of the solutions. For low Reynolds numbers, the solution is stationary; for moderate Reynolds numbers, it is time periodic. For high Reynolds numbers, the solution is neither stationary nor time periodic: the solution becomes chaotic. Of the small vortices, the merging and the splitting, the appearance and the disappearance, and, sometime, the dragging away from one corner to another and the impeding of the merging—these mark the route to chaos. For high Reynolds numbers, over weak fundamental frequencies appears a very low frequency dominating the spectra—this very low frequency being weaker than clear-cut fundamental frequencies seems an indication that the global attractor has been attained. The global attractor seems reached for Reynolds numbers up to Re=15,000. This is the lid-driven square cavity flow; the motivations for studying this flow are recalled in the Introduction.

AMS subject classifications: 76M20, 76D05, 76F06, 37N10

Key words: Finite differences, staggered marker-and-cell (MAC) mesh, incremental unknowns, generalized Stokes equations, incompressible Navier-Stokes equations, chaos.

1 Introduction

The square: the simplest shape—the flow: unexpected and complicated long-term dynamic behavior and the global attractor persisting at extremely large time *t*—this is the lid-driven square cavity flow—an almost fictitious flow [27]—solved many times by various techniques: [1, 10, 19, 21, 23, 26, 35], their results sometime agreeing, sometime disagreeing.

*Corresponding author. *Email address:* `sgarcia@uctemuco.cl` (S. Garcia)

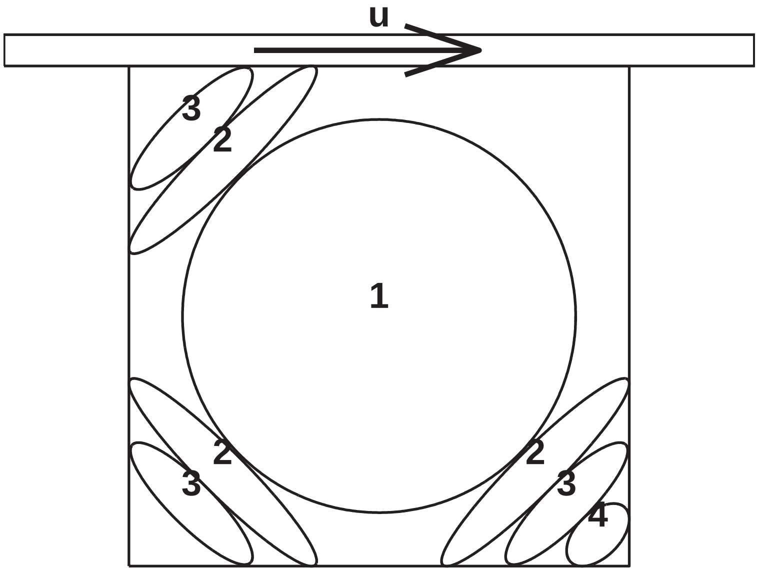

Figure 1: The lid-driven square cavity flow.

The domain is the unit square cavity, and the viscous incompressible flow is governed by the two-dimensional time-dependent incompressible Navier-Stokes equations (NSE) [33] and driven by the upper wall, see Fig. 1. Here, we consider the nondimensionalized NSE in primitive variables with Dirichlet boundary conditions over the domain $\Omega =]0,1[\times]0,1[$; that is

$$\begin{cases} \dfrac{\partial \mathbf{u}}{\partial t} - \nu\Delta\mathbf{u} + c(\mathbf{u},\mathbf{u}) + \nabla p = \mathbf{f} & \text{in } \Omega,\ t>0, \\ \nabla\cdot\mathbf{u} = 0 & \text{in } \Omega, \\ \mathbf{u} = \boldsymbol{\varphi} & \text{on } \Gamma = \partial\Omega, \\ \mathbf{u}(\mathbf{x},0) = \mathbf{u}_0(\mathbf{x}) & \text{in } \Omega, \end{cases} \tag{1.1}$$

where $\mathbf{u}$ is the velocity, p is the pressure, $\nu > 0$ is the kinematic viscosity, $\mathrm{Re} = \nu^{-1}$ is the Reynolds number, $\mathbf{f}$ is the external force, and $c(\mathbf{u},\mathbf{v}) = (\mathbf{u}\cdot\nabla)\mathbf{v}$ represents the convection term. Here, we set $\mathbf{f} = \mathbf{0}$ and consider the boundary conditions

$$\begin{cases} \mathbf{u}(\mathbf{x},\cdot) = (1,0) & \text{if } \mathbf{x} \in \text{upper wall}, \\ \mathbf{u}(\mathbf{x},\cdot) = \mathbf{0} & \text{if } \mathbf{x} \in \text{left, bottom, or right wall}. \end{cases} \tag{1.2}$$

An unexpected balance of viscous and pressure forces makes the fluid to turn into the square cavity. The properties of these forces depending upon the Reynolds number, a hierarchy of vortices develops—the large clockwise-rotating primary vortex (1), whose location occurs toward the geometric center of the square cavity, and several small vortices: the counterclockwise-rotating secondary vortices (2), the clockwise-rotating tertiary vortices (3), the counterclockwise-rotating quaternary vortices (4), whose locations occur at the three relevant corners of the square cavity: bottom left (BL), bottom right (BR), and top left (TL), and appear hierarchically at the inclined ellipses as in Fig. 1.

Specifically, at the three relevant corners of the square cavity and at each level, secondary, tertiary, and quaternary, one or two small vortices develop. If there is only one small vortex, this is named after the corresponding corner and the corresponding level, subscript; e.g., the bottom right tertiary vortex is named BR_3. If there are two small vortices, one occurs on the up (U) side of the inclined ellipse; the other, on the down (D) side. The corresponding letter U, D is added to the left of its name; e.g., the two bottom right secondary vortices are named UBR_2 and DBR_2.

But, the agreement and disagreement in the results of so many authors, what is it about?

In the first place, it is about the quantities obtained. Firstly, we consider the characteristics of BR_2. For Re = 1,000, our results agree with those obtained by all authors except [21]. The results obtained in [21] are different from all the other published results; in particular, the strength of BR_2 is weaker, for the most part. For Re = 5,000, our results agree with those obtained in [1, 10] and [19] and differ with those obtained in [21, 35]. The results displayed in [21, 35] are different from all the others: according to [21], the strength of BR_2 is weaker; according to [35], stronger, for the most part. Secondly, we consider the characteristics of the primary vortex. For Re=5,000, Re=7,500, Re=10,000, and Re=12,500, our results agree with those obtained in [1,10], and [23] and are different from those obtained in [19] where the strength of the primary vortex is systematically weakened. The results obtained in [21,35], and [26] differ significantly from those obtained by the other authors, the strength of the primary vortex being substantially weaker.

In the second place, it is about the quality of the solutions obtained. In [1,10,19,23,26, 35], the authors consider the stationary NSE, but in [21] and in the present research, the time-dependent NSE; so that qualitative comparisons are possible with [21]. In [21] the author reports stationary solutions in a row from Re=100 to Re=7,500, and time periodic solutions in a row for Re=10,000 and Re=12,500. Notwithstanding, we report stationary solutions in a row from Re=100 to Re=5,000—and time periodic solutions in a row from Re = 7,500 to Re = 12,500, this kind of solutions occurring for smaller Reynolds numbers in the present research.

On the other hand, we know that the dynamical system associated with the two-dimensional NSE possesses a global attractor, see [32, page 104] and the references therein, typically a complicated set—perhaps a fractal set; when the time t is large, $\mathbf{u}(\cdot,t)$ wanders around the global attractor, and the complicated convolutions of this set cause the complicated form of the flow, explaining its chaotic appearance.

For the lid-driven cavity flow, we aim to reach the picture of the global attractor and record the long-term dynamic behavior of the small vortices in the flow, which should decay exponentially toward a small value [11]. Immediately, a serious difficulty arises—the global attractor persists for extremely large times t. The temporal and spatial methodology used to perform the long-term integration should be extremely efficient and accurate.

And we would like to do the computations with large time steps. Therefore, further questions arise: what is the effect of the time step and of the inherent temporal errors in the computed solution, and how to know when the global attractor has been reached?

A new combination of known methods is used to compute the solutions of the NSE: the linear Linθ^*-scheme, the projection method, the Conjugate Gradient method, the Bi-CGSTAB method, the Fast Fourier Transform method—and incremental unknowns as a spatial preconditioner. The temporal and spatial methodology is accurate and efficient.

The incremental unknowns—first introduced by Temam [31] through approximate inertial manifolds and spatial multilevel finite-difference discretizations—are a natural tool to study the long-term dynamic behavior of nonlinear dissipative evolutionary equations, see, e.g., [2–8, 12–18, 24].

Ranging from $\mathrm{Re}=100$ to $\mathrm{Re}=20{,}000$, several computational experiments are conducted, Re being the Reynolds number. The primary vortex stays put. For low Reynolds numbers, the solution is stationary; for moderate Reynolds numbers, it is time periodic. For high Reynolds numbers, the solution is neither stationary nor time periodic: the solution becomes chaotic. Of the small vortices, the merging and the splitting, the appearance and the disappearance, and, sometime, the dragging away from one corner to another and the impeding of the merging—these mark the route to chaos. For high Reynolds numbers, over weak fundamental frequencies appears a very low frequency dominating the spectra—this very low frequency being weaker than clear-cut fundamental frequencies seems an indication that the global attractor has been attained. The global attractor seems reached for Reynolds numbers up to $\mathrm{Re}=15{,}000$. This is the lid-driven square cavity flow.

There are controversies about such two-dimensional flows, see, e.g., [27, page 105], whether or not they are physically relevant to turbulence. We do not enter into this controversy here. It seems to us that the problem studied can somehow model the central part of the flow in a long cavity (long in the z-direction) driven by an outside flow (dominantly in the x-direction). It is also a relevant study for the understanding of the corresponding two-dimensional global attractor [32, p. 104] which has not been proven to be trivial.

This article is organized as follows. In Section 2, we consider the temporal and spatial discretizations of the NSE and discuss the numerical resolution of the underlying linear systems. In Section 3, ranging from $\mathrm{Re}=100$ to $\mathrm{Re}=20{,}000$, several computational experiments are conducted. Finally, in Section 4, we summarize our conclusions.

2 Temporal and spatial discretization

Here, we consider the temporal and spatial discretization of the NSE and discuss the numerical resolution of the underlying linear systems.

Algorithm 2.1: The nonlinear θ-scheme and the linear Linθ^*-scheme.

Set $\mathbf{u}^0 = \mathbf{u}_0$
for $n = 0,1,2,\cdots$
  Solve the intermediate quantities $\mathbf{u}^{n+\theta}$, $p^{n+\theta}$:

$$\frac{\mathbf{u}^{n+\theta}-\mathbf{u}^n}{\theta\Delta t} - \alpha\nu\Delta\mathbf{u}^{n+\theta} + \nabla p^{n+\theta} = \mathbf{f}^{n+\theta} + \beta\nu\Delta\mathbf{u}^n - c(\mathbf{u}^n,\mathbf{u}^n) \text{ in } \Omega,$$
$$\nabla\cdot\mathbf{u}^{n+\theta} = 0 \text{ in } \Omega,$$
$$\mathbf{u}^{n+\theta} = \boldsymbol{\varphi}^{n+\theta} \text{ on } \Gamma = \partial\Omega,$$

  Solve the intermediate quantities $\mathbf{u}^{n+1-\theta}$, $p^{n+1-\theta}$:

$$\frac{\mathbf{u}^{n+1-\theta}-\mathbf{u}^{n+\theta}}{(1-2\theta)\Delta t} - \beta\nu\Delta\mathbf{u}^{n+1-\theta} + c(\mathbf{u}^*,\mathbf{u}^{n+1-\theta}) = \mathbf{f}^{n+1-\theta} + \alpha\nu\Delta\mathbf{u}^{n+\theta} - \nabla p^{n+\theta} \text{ in } \Omega,$$
$$\mathbf{u}^{n+1-\theta} = \boldsymbol{\varphi}^{n+1-\theta} \text{ on } \Gamma = \partial\Omega,$$

  Solve the ultimate quantities $\mathbf{u}^{n+1}$, p^{n+1}:

$$\frac{\mathbf{u}^{n+1}-\mathbf{u}^{n+1-\theta}}{\theta\Delta t} - \alpha\nu\Delta\mathbf{u}^{n+1} + \nabla p^{n+1} = \mathbf{f}^{n+1} + \beta\nu\Delta\mathbf{u}^{n+1-\theta} - c(\mathbf{u}^*,\mathbf{u}^{n+1-\theta}) \text{ in } \Omega,$$
$$\nabla\cdot\mathbf{u}^{n+1} = 0 \text{ in } \Omega,$$
$$\mathbf{u}^{n+1} = \boldsymbol{\varphi}^{n+1} \text{ on } \Gamma = \partial\Omega.$$

end

2.1 The temporal discretization

The nonlinear θ-scheme [20] and the linear Linθ^*-scheme [28] are used for the temporal discretization of the NSE. These numerical schemes are described in Algorithm 2.1. The quantities $\mathbf{f}^\tau$, $\boldsymbol{\varphi}^\tau$ are the quantities $\mathbf{f}$, $\boldsymbol{\varphi}$ at time τ.

The nonlinear θ-scheme and the linear Linθ^*-scheme are set by choosing the parameters θ,α,β and the quantity $\mathbf{u}^*$. The choices are highlighted in Table 1: for $\mathbf{u}^* = \mathbf{u}^{n+1-\theta}$, we obtain the nonlinear θ-scheme; for

$$\mathbf{u}^* = \frac{2\theta-1}{\theta}\mathbf{u}^n + \frac{1-\theta}{\theta}\mathbf{u}^{n+\theta},$$

we obtain the linear Linθ^*-scheme.

The linear Linθ^*-scheme possesses the same advantages as the nonlinear θ-scheme: second-order accuracy in time—detachability of the incompressibility and the nonlinearity—unconditional stability—invariance of the linear systems throughout the temporal iterations. Furthermore, it adds a crucial advantage: the replacement of a nonlinear elliptic equation by a linear elliptic equation with variable coefficients. The linear Linθ^*-scheme has been our choice for the temporal discretization.

In practice, two generalized Stokes equations (GSE) and one linear elliptic equation with variable coefficients must be solved at each temporal iteration. And these equations have then to be discretized at present in space, a question that we now address.

Table 1: The nonlinear θ-scheme and the linear Linθ^*-scheme.

	Parameters			
Acronym	θ	α	β	$\mathbf{u}^*$
θ	$1-\frac{1}{\sqrt{2}}$	$\frac{1-2\theta}{1-\theta}$	$\frac{\theta}{1-\theta}$	$\mathbf{u}^{n+1-\theta}$
Linθ^*	$1-\frac{1}{\sqrt{2}}$	$\frac{1-2\theta}{1-\theta}$	$\frac{\theta}{1-\theta}$	$\frac{2\theta-1}{\theta}\mathbf{u}^n+\frac{1-\theta}{\theta}\mathbf{u}^{n+\theta}$

2.2 The spatial discretization

First, we consider the generalized Stokes equations (GSE) and then we treat the linear elliptic equation with variable coefficients.

2.2.1 The generalized Stokes equation

Here, we consider the following GSE in primitive variables with Dirichlet boundary conditions over the domain $\Omega =]0,1[\times]0,1[$

$$\begin{cases} -\nu\Delta u+\gamma u+\dfrac{\partial p}{\partial x}=f, \\ -\nu\Delta v+\gamma v+\dfrac{\partial p}{\partial y}=g, \\ \dfrac{\partial u}{\partial x}+\dfrac{\partial v}{\partial y}=0, \\ u\big|_\Gamma=\varphi, \quad v\big|_\Gamma=\psi, \end{cases} \tag{2.1}$$

where $\mathbf{u}=(u,v)$ is the velocity, p is the pressure, $\mathbf{f}=(f,g)$ is the external force, $\nu>0$ is the kinematic viscosity, and $\gamma\geq 0$ is a given constant.

Its spatial discretization is performed on a staggered marker-and-cell (MAC) mesh by finite-differences [22]. The mesh size in both directions is $h=1/N$, where N is a non-negative integer. An $(N-1)\times N$ (classical mesh) $\times$ (staggered mesh) is used to discretize the first component of the velocity; an $N\times(N-1)$ (staggered mesh) $\times$ (classical mesh), to discretize the second component; and an $N\times N$ (staggered mesh) $\times$ (staggered mesh), to discretize the pressure.

Using lexicographical order for the unknown u, transposed lexicographical order for the unknown v, and lexicographical order for the unknown p, we obtain the spatial discretization in block form of the GSE [16]:

$$\begin{bmatrix} \mathsf{A} & \mathsf{B} \\ -\mathsf{B}^T & O \end{bmatrix}\begin{bmatrix} \mathbf{u} \\ p \end{bmatrix}=\begin{bmatrix} \mathbf{f} \\ z \end{bmatrix}, \tag{2.2}$$

where

$$\mathsf{A}=\begin{bmatrix}\mathcal{A}_\gamma & O\\ O & \mathcal{A}_\gamma\end{bmatrix},\qquad \mathsf{B}=\begin{bmatrix}\mathcal{B}\\ \mathcal{T}^T\overline{\mathcal{B}}\end{bmatrix},\qquad \mathbf{u}=\begin{bmatrix}u\\ \overline{v}\end{bmatrix},\qquad \mathbf{f}=\begin{bmatrix}\check{f}\\ \mathcal{T}^T\check{g}\end{bmatrix}, \tag{2.3}$$
$$\mathcal{A}_\gamma=-\nu\boldsymbol{\Delta}_h^{\mathsf{s}}+\gamma I_N\bigotimes I_{N-1},\qquad \mathcal{B}=I_N\bigotimes\delta_{\frac{h}{2}},\qquad \overline{\mathcal{B}}=\delta_{\frac{h}{2}}\bigotimes I_N,$$
$$\boldsymbol{\Delta}_h^{\mathsf{s}}=I_N\bigotimes\Delta_h+\Delta_h^{\mathsf{s}}\bigotimes I_{N-1}.$$

The operators $\boldsymbol{\Delta}_h^{\mathsf{s}},\Delta_h^{\mathsf{s}},\Delta_h$ are the two-dimensional staggered, the one-dimensional staggered, and the classical finite-difference Laplace operators with Dirichlet boundary conditions,

$$\Delta_h=\frac{1}{h^2}\begin{bmatrix}-2 & 1 & & & \\ 1 & -2 & 1 & & \\ & \ddots & \ddots & \ddots & \\ & & 1 & -2 & 1\\ & & & 1 & -2\end{bmatrix},\qquad \Delta_h^{\mathsf{s}}=\frac{1}{h^2}\begin{bmatrix}-3 & 1 & & & \\ 1 & -2 & 1 & & \\ & \ddots & \ddots & \ddots & \\ & & 1 & -2 & 1\\ & & & 1 & -3\end{bmatrix}.$$

The operator $\delta_{\frac{h}{2}}$ is the centered second-order finite-difference with halved mesh size $h/2$ for the first derivative:

$$\delta_{\frac{h}{2}}=\frac{1}{h}\begin{bmatrix}-1 & 1 & & & & \\ & -1 & 1 & & & \\ & & \ddots & \ddots & & \\ & & & -1 & 1 & \\ & & & & -1 & 1\end{bmatrix}.$$

Hereafter, we write $v=\mathcal{T}\overline{v}$, where $\mathcal{T}$ is the transposed permutation matrix. The operator I_J is the identity matrix of order J. Finally, the quantities $\check{f}$ and $\check{g}$ are the finite-difference discretizations of the right-hand side of the equations with, near the boundary, some terms coming from the finite-difference discretizations of the Laplace operator and involving the Dirichlet boundary conditions (boundary and extrapolated values). The quantity z is the finite-difference discretization of the *zero* function with, near the boundary, some terms coming from the finite-difference discretization of the divergence operator and involving the Dirichlet boundary conditions (boundary values).

To solve the GSE, we use the projection method, see [25] and the references therein. In the end, we uncouple the variables $\mathbf{u},p$ to obtain a linear system for the velocity:

$$\mathsf{PAP}\mathbf{u}=\mathsf{P}\left(\mathbf{f}+\mathsf{AB}\left(\mathsf{B}^T\mathsf{B}\right)^{-1}z\right). \tag{2.4}$$

Here, P is the orthogonal projector onto the null space of B^T:

$$\mathsf{P}=I-\mathsf{BB}^{\dagger}=I-\mathsf{B}\left(\mathsf{B}^T\mathsf{B}\right)^{-1}\mathsf{B}^T, \tag{2.5}$$

where I is the identity matrix and $\mathsf{B}^\dagger$ is the Moore-Penrose inverse of B:

$$\mathsf{B}^\dagger = \left(\mathsf{B}^T\mathsf{B}\right)^{-1}\mathsf{B}^T. \tag{2.6}$$

The matrix PAP is symmetric positive semidefinite, and $\mathsf{null}(\mathsf{PAP}) = \mathsf{null}(\mathsf{P}) = \mathsf{range}(\mathsf{B})$. Then, the linear system (2.4) is solvable. And to solve it, we apply the Conjugate Gradient (CG) method [9] to the linear system

$$\mathsf{PA}\mathbf{u} = \mathsf{P}\mathbf{f},$$

for the unknown $\mathbf{u}$ with $\mathsf{B}^T\mathbf{u} = -z$.

Each CG iteration requires computing the action of the projector P: solving a linear system $\mathsf{B}^T\mathsf{B}\,\zeta = \mathsf{B}^T d$ being the most difficult operation, other significant operations being matrix-vector products.

But, solving a linear system $\mathsf{B}^T\mathsf{B}\,\zeta = \mathsf{B}^T d$, is this a simple computational task? See, [25, p. 207]. Here, the matrix $\mathsf{B}^T\mathsf{B}$ reads

$$\mathsf{B}^T\mathsf{B} = I_n \bigotimes \delta^T_{\frac{h}{2}}\delta_{\frac{h}{2}} + \delta^T_{\frac{h}{2}}\delta_{\frac{h}{2}} \bigotimes I_n = -\boldsymbol{\Delta}^{\mathsf{n}}_h, \tag{2.7}$$

where the operator $\boldsymbol{\Delta}^{\mathsf{n}}_h$ is the two-dimensional staggered finite-difference Laplace operator with Neumann boundary conditions [16]. Furthermore, we have that $(\mathsf{B}^T d, \mathbf{1}) = (d, \mathsf{B}\mathbf{1}) = 0$, where $\mathbf{1}$ is the unit function and $(\cdot,\cdot)$ is the scalar product of the Hilbert space $L^2(\Omega)$.

Therefore, solving a linear system $\mathsf{B}^T\mathsf{B}\,\zeta = \mathsf{B}^T d$ amounts to solving a two-dimensional discrete Poisson equation with Neumann boundary conditions—indeed, a simple computational task, performed by a direct Fast Fourier Transform (FFT) method [30].

Finally, the pressure is computed from the equation

$$p = \mathsf{B}^\dagger(\mathbf{f} - \mathsf{A}\mathbf{u}). \tag{2.8}$$

2.2.2 The linear elliptic equation with variable coefficients

Here, we consider the following linear elliptic equation with variable coefficients in primitive variables with Dirichlet boundary conditions over the domain $\Omega = \,]0,1[\times]0,1[$

$$\left|\begin{array}{l} -\nu\Delta u + \mu u + u^*\dfrac{\partial u}{\partial x} + v^*\dfrac{\partial u}{\partial y} = f, \\ -\nu\Delta v + \mu v + u^*\dfrac{\partial v}{\partial x} + v^*\dfrac{\partial v}{\partial y} = g, \\ u\big|_\Gamma = \varphi, \quad v\big|_\Gamma = \psi, \end{array}\right. \tag{2.9}$$

where $\mathbf{u} = (u,v)$ is the velocity, p is the pressure, $\mathbf{f} = (f,g)$ is the external force, $\nu > 0$ is the kinematic viscosity, and $\mu \geq 0$ is a given constant. Here, the quantity $\mathbf{u}^* = (u^*,v^*)$ is known and computed from the relation

$$\mathbf{u}^* = \frac{2\theta - 1}{\theta}\mathbf{u}^n + \frac{1-\theta}{\theta}\mathbf{u}^{n+\theta}, \qquad \theta = 1 - \frac{1}{\sqrt{2}}. \tag{2.10}$$

The discretization is performed on an $(N-1)\times N$ (classical mesh) $\times$ (staggered mesh) by finite differences. To discretize the convection terms, we use uncentered second-order first finite-differences:

$$\rho(x,y)\frac{\partial w}{\partial x}(x,y)\approx\rho(x,y)\nabla_{x,\rho(x,y)}w(x,y),$$

where $\nabla_{x,\rho(x,y)}w(x,y)$ is the partial uncentered second-order first finite-difference with respect to x. The ordinary uncentered second-order first finite-difference with respect to x is

$$\nabla_{\rho(x)}w(x)=\begin{cases}\dfrac{3w(x)-4w(x-h)+w(x-2h)}{2h}, & \text{if } \rho(x)\geq 0,\\ -\dfrac{3w(x)-4w(x+h)+w(x+2h)}{2h}, & \text{if } \rho(x)<0.\end{cases}$$

The discrete equation reads

$$\begin{cases}-\nu\boldsymbol{\Delta}_h^{\mathsf{s}}u+\mu u+u^*\nabla_{x,u^*}u+\overline{\overline{v^*}\nabla_{x,\overline{v^*}}\overline{u}}=\check{f}(u^*,\overline{v^*}),\\ -\nu\boldsymbol{\Delta}_h^{\mathsf{s}}\overline{v}+\mu\overline{v}+\overline{u^*\nabla_{x,u^*}v}+\overline{v^*}\nabla_{x,\overline{v^*}}\overline{v}=\overline{\breve{g}(u^*,\overline{v^*})}.\end{cases} \tag{2.11}$$

The quantities $\check{f}(u^*,\overline{v^*}),\overline{\breve{g}(u^*,\overline{v^*})}$ are the finite-difference discretizations of the right-hand sides of the equations with, near the boundary, some terms coming from the finite-difference discretization of the Laplace operator and of the convection terms, related to the Dirichlet boundary conditions (boundary and extrapolated values)—and the quantity $\mathbf{u}^*=(u^*,v^*)$ (values near the boundary).

The matrices being nonsymmetric, we solve the linear systems before by the preconditioned Bi-CGSTAB method [34], using incremental unknowns in the preconditioner [16]. To build up the block diagonal (scaling) preconditioning matrix, we neglect the variable coefficients and consider only the block diagonal part of the incremental unknowns matrix associated to the operator $\mathcal{A}_\mu=-\nu\boldsymbol{\Delta}_h^{\mathsf{s}}+\mu I$. Furthermore, at the coarsest level, some terms are added; others, dropped, making $\alpha_{\mathsf{last}}=\alpha,\gamma_{\mathsf{first}}=\gamma_{\mathsf{last}}=\gamma$, see [16, p. 458]. This approximation allows us to switch from direct LU decomposition methods to direct FFT methods [29] in the preconditioner.

3 Computational experiments

Ranging from Re$=$100 to Re$=$20,000, several computational experiments are conducted: long-term integration—mesh-size and time-step refinement analysis—change of the initial condition—detailed comparisons of quantities. The global attractor seems reached for Reynolds numbers up to Re$=$15,000.

3.1 Preliminaries

To do the computations, we take $N=128$ and $N=256$. For the incremental unknowns setup, we always choose $\text{ł}=2$, where ł is the number of levels; so we choose $M=64$ and

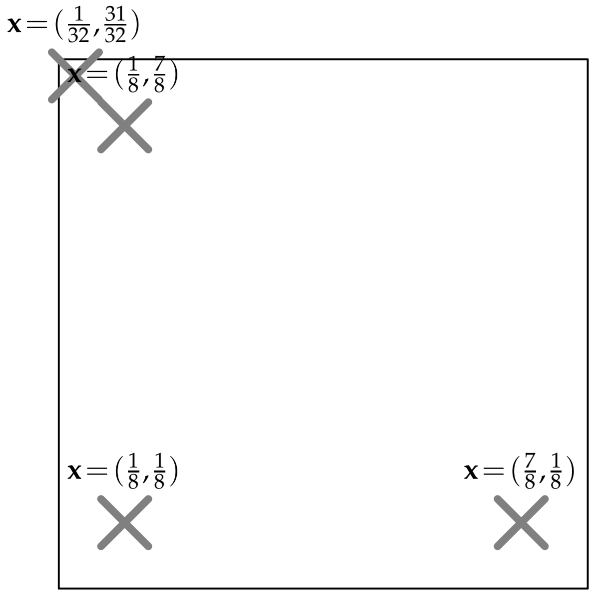

Figure 2: The three relevant corners of the square cavity.

$M = 128$, where M determines the coarsest mesh size. For $\text{Re} \leq 5{,}000$, the initial condition $\mathbf{u}_0$ is the solution of the Stokes equation, that is, the GSE with $\gamma = 0$, at the same Reynolds number; for $\text{Re} > 5{,}000$, it is the last computed solution of the NSE at the Reynolds number considered just before.

To perceive the long-term dynamic behavior of the flow, we will use phase diagrams. Using the time step $\Delta t = 4h$, the time t_∞ is a large time for which in the first instance a solution has been computed, a large time where the global attractor seems attained. The complete phase diagram at the point $\mathbf{x}$ is the plot of the values $(u(\mathbf{x},t), v(\mathbf{x},t))$, from $t=0$ to $t=t_\infty$. The detailed phase diagram at the point $\mathbf{x}$ is the plot of the values $(u(\mathbf{x},t), v(\mathbf{x},t))$ in a 2×2 windowed matrix W displayed in row-major order by discarding more and more portions of time as $t \longrightarrow t_\infty$: in W(1,1) appears the complete phase diagram at the point $\mathbf{x}$; in W(1,2), the plot of the values $(u(\mathbf{x},t), v(\mathbf{x},t))$ from $t = t_1$ to $t = t_\infty$; in W(2,1), the plot of the values $(u(\mathbf{x},t), v(\mathbf{x},t))$ from $t = t_2$ to $t = t_\infty$; in W(2,2), the plot of the values $(u(\mathbf{x},t), v(\mathbf{x},t))$ from $t = t_3$ to $t = t_\infty$. Here, t_1, t_2, t_3 are chosen such that $t = 0 \lll t_1 \lll t_2 \lll t_3$ and $t_3 \approx t_\infty$, to better perceive the long-term dynamic behavior of the flow.

Phase diagrams will be considered at the three relevant corners of the square cavity: at the bottom left corner, $\mathbf{x} = (\frac{1}{8}, \frac{1}{8})$, at the bottom right corner, $\mathbf{x} = (\frac{7}{8}, \frac{1}{8})$, and at the top left corner, $\mathbf{x} = (\frac{1}{8}, \frac{7}{8}), (\frac{1}{32}, \frac{31}{32})$, see Fig. 2. The complete phase diagram at the three relevant corners of the square cavity is the simultaneous display of the complete phase diagram at the points $\mathbf{x} = (\frac{1}{8}, \frac{1}{8})$, $(\frac{7}{8}, \frac{1}{8})$, $(\frac{1}{8}, \frac{7}{8})$, presented in a 2×2 windowed matrix W displayed in row-major order by location: in W(2,1) is the complete phase diagram at the point $\mathbf{x} = (\frac{1}{8}, \frac{1}{8})$; in W(2,2), the complete phase diagram at the point $\mathbf{x} = (\frac{7}{8}, \frac{1}{8})$; in W(1,1), the complete phase diagram at the point $\mathbf{x} = (\frac{1}{8}, \frac{7}{8})$. W(1,2) is empty.

To assess the end of the computations, that is, to assess if the global attractor has been

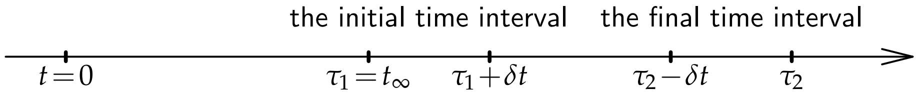

Figure 3: The time-step refinement analysis.

reached, we carry out a time-step refinement analysis. With the time step $\Delta t=4h$, the computations are performed from $t=0$ to $t=t_\infty$. Then, the computations are continued from $t=\tau_1=t_\infty$ to $t=\tau_2$, where $\tau_1 \lll \tau_2$, with four time steps: $\Delta t=h$, $\Delta t=2h$, $\Delta t=3h$, and $\Delta t=4h$—always starting with the same initial condition, the last solution computed at time $t=t_\infty$ with the time step $\Delta t=4h$. Two time intervals are fixed: the initial time interval $[\tau_1,\tau_1+\delta t]$ and the final time interval $[\tau_2-\delta t,\tau_2]$, where δt is a lapse of time, $\delta t=93.75$, always, see Fig. 3.

For an interval $[t_1,t_2]$, the oscillograms of the kinetic energy and, at any relevant corner of the square cavity, the phase diagrams, and their corresponding power spectra with the four time steps—$\Delta t=h$, $\Delta t=2h$, $\Delta t=3h$, and $\Delta t=4h$—are presented in a 1×2 windowed matrix W: in $\mathsf{W}(1,1)$ are the oscillograms of the kinetic energy or the phase diagrams; in $\mathsf{W}(1,2)$, their corresponding power spectra, their likeness or unlikeness allowing to assess the end or extent of the computations: the reaching or not of the global attractor. The kinetic energy of the flow is $\mathsf{E}_{\mathbf{u}}(t)=\|\mathbf{u}(\cdot,t)\|^2_{\ell_2}$. Here, the oscillogram of the kinetic energy is the plot of the values $(t,\mathsf{E}_{\mathbf{u}}(t))$ from $t=t_1$ to $t=t_2$. The phase diagram at the point $\mathbf{x}$ is the plot of the values $(u(\mathbf{x},t),v(\mathbf{x},t))$ from $t=t_1$ to $t=t_2$. The time-step refinement analysis is displayed in Fig. 11, the initial time interval, and in Fig. 12, the final time interval.

Throughout, we will stick to a gray-color usage: a 0 gray (black) line means computations performed with the time step $\Delta t=4h$, displayed first; a 0.25 gray line, $\Delta t=3h$, second; a 0.5 gray line, $\Delta t=2h$, third; a 0.75 gray line, $\Delta t=h$, last, unless otherwise specified.

To perceive the geometrical structure of the flow and the associated physics, we will consider sequences of streamlines. For time periodic solutions, the computations will be performed with the time step $\Delta t=4h$. Once the time periodic solution has been reached, two consecutive relative maxima are identified. Let us assume they occur at time t_1 and time t_2, with $t_1<t_2$. Let J be the number of temporal iterations with the time step $\Delta t=4h$ which are needed to go from $t=t_1$ to $t=t_2$. A complete cycle of streamlines is the plot of the streamlines in a 4×3 windowed matrix W displayed in row-major order for the solutions computed at the sequence of times $t=t_1+j\times\mathsf{ceil}(J/12)$, for $j=0,\cdots,11$, where ceil rounds toward infinity. The time $t=t_1+12\times\mathsf{ceil}(J/12)$ may not be exactly the time $t=t_2$, but it will be very close past the time t_2.

For chaotic solutions, the computations will be performed with the time step $\Delta t=h$, after the time t_∞. Once the global attractor or a large time is reached, a large initial time T with $t_\infty \lll T$ is chosen to better highlight distinctive features of the flow. A partial sequence of streamlines is the plot of the streamlines in a 4×3 windowed matrix W displayed in row-major order for the solutions computed at the sequence of times

$t = T + j \times 20 \times h$, for $j = 0, \cdots, 11$. The levels for the streamlines are:

1. $\pm 1 \times \frac{1}{10^i}$, $\pm 3 \times \frac{1}{10^i}$, for $i = 2, \cdots, 15$;
2. 0;
3. $-12 \times \frac{1}{10^2} - i \times \frac{1}{10^2}$, for $i = 0, \cdots, 10$.

3.2 Stationary solutions

For Re = 100, Re = 1,000, Re = 3,200, and Re = 5,000, the solution is stationary.

The case Re = **5,000.** The long-term dynamic behavior of the flow at the three relevant corners of the square cavity is unstructured in the mid term and structured in the long term—and the large time step $\Delta t = 4h$ chosen makes this chaotic in the end. First, the long-term integration is performed with the time step $\Delta t = h$ (black line); then, with the time step $\Delta t = 4h$ (light gray line). In Fig. 4, we display the detailed phase diagram at the point $\mathbf{x} = (\frac{7}{8}, \frac{1}{8})$. Computed with the time step $\Delta t = h$, the long-term dynamic behavior is sharp throughout; computed with the time step $\Delta t = 4h$, it stays very close to the former everywhere—but this is chaotic in the end. Notwithstanding, the long-term integration performed with the time step $\Delta t = 4h$ preserves accuracy, the distance between the starting points in Fig. 4, bottom right, being

$$d = 8.49 \times 10^{-7} = \mathcal{O}(10^{-7}).$$

Now, some contrasts. In Fig. 5 we display the detailed phase diagram at the point $\mathbf{x} = (\frac{7}{8}, \frac{1}{8})$: the linear Lin$\theta^*$-scheme (black line) versus the nonlinear θ-scheme (light gray line). The nonlinear θ-scheme produces a blurred long-term dynamic behavior, whereas the linear Linθ^*-scheme draws a sharp one. These numerical results favor the use of the linear Linθ^*-scheme over the nonlinear θ-scheme. Notwithstanding, the nonlinear θ-scheme preserves accuracy, the distance between the end points in Fig. 5 bottom right being

$$d = 4.16 \times 10^{-5} = \mathcal{O}(10^{-5}).$$

At this point in time, the mesh-size refinement analysis. In Fig. 6, we display the complete phase diagram at the point $\mathbf{x} = (\frac{7}{8}, \frac{1}{8})$. First, the long-term integration is performed with $N = 128$ and $\Delta t = 4h$, looking inclined; then, it is achieved with $N = 256$ and $\Delta t = h$, looking symmetrical. Qualitatively, they behave similarly. To some extent, the long-term integration performed with $N = 128$ and $\Delta t = 4h$ preserves accuracy, the distance between the end points in Fig. 6 being

$$d = 7.23 \times 10^{-3} = \mathcal{O}(10^{-3}).$$

Now, the time-step refinement analysis, see Fig. 7: the initial interval (top) and the final interval (bottom). Here, we take $\tau_1 = 2{,}062.5$ and $\tau_2 = 2{,}453.1094$. On the initial interval and on the final interval with $\Delta t = 4h$, the oscillograms of the kinetic energy and the corresponding power spectra resemble. Indeed, the global attractor has been attained.

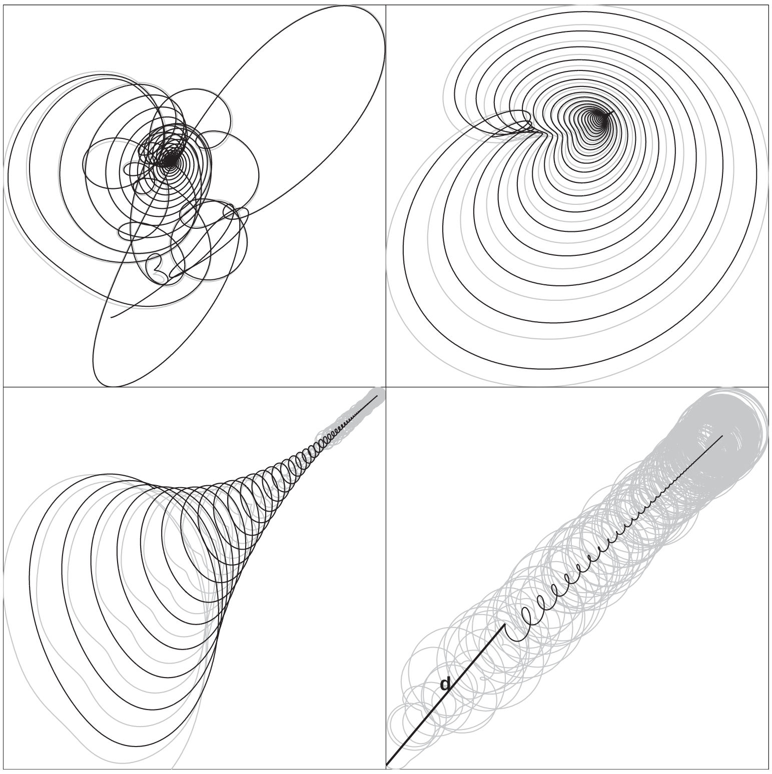

Figure 4: The detailed phase diagram at the point $\mathbf{x}=(\frac{7}{8},\frac{1}{8})$. Re$=$5,000. $N=256$. $\Delta t=h$ (black line). $\Delta t=4h$ (light gray line).

On the final interval, three fundamental frequencies—$f_4=0.896$, $f_5=1.2373$, $f_6=1.536$—with amplitudes of the order $\mathcal{O}(10^{-8})$ set the pace, and a very low frequency—$f_1=0.0427$—and noise-like frequencies—$f_2=0.2987$, $f_3=0.5973$—with amplitudes of the order $\mathcal{O}(10^{-9})$ push or pull while active, causing feeble chaotic behavior.

On the initial interval with $\Delta t=h$, $\Delta t=2h$, and $\Delta t=3h$, the oscillograms of the kinetic energy, see Fig. 7 (top left), stay very close for a short period of time to the one with $\Delta t=4h$. Then, they approach the same stationary solution. On the final interval the oscillograms of the kinetic energy, see Fig. 7 (bottom left), corroborate this behavior. The feebly chaotic solution computed with the time step $\Delta t=4h$ fluctuates around the stationary solution computed with the time steps $\Delta t=h$, $\Delta t=2h$, and $\Delta t=3h$. These fluctuations, see Fig. 7 (left), are of the order $\mathcal{O}(10^{-4})$, preserving accuracy, notwithstanding.

Finally, the geometrical structure of the flow and the associated physics. In Fig. 8 we display the streamlines of the stationary solutions. For Re$=100$, the location of the primary vortex appears toward the top right corner; for Re increasing, it moves toward the geometric center of the square cavity. Secondary and tertiary vortices emerge at the three relevant corners of the square cavity.

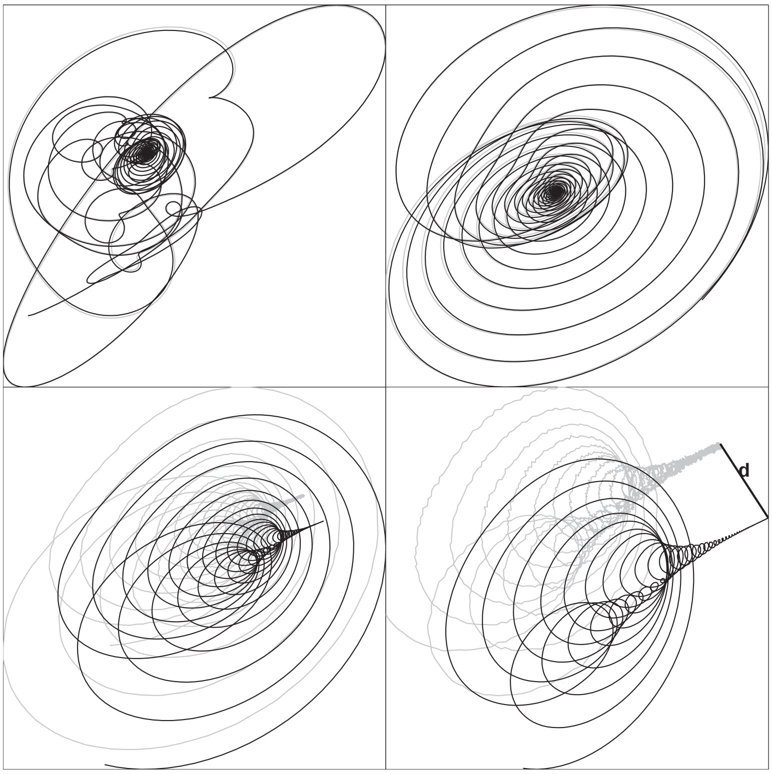

Figure 5: The linear Linθ^*-scheme (black line) versus the nonlinear θ-scheme (light gray line). $\mathrm{Re}=5{,}000$. $N=128$.

3.3 Time periodic solutions

For $\mathrm{Re}=7{,}500$, $\mathrm{Re}=10{,}000$, and $\mathrm{Re}=12{,}500$, the solution is time periodic.

The dynamic behavior of the flow at the three relevant corners of the square cavity is unstructured in the mid term and structured in the long term—indeed, this is time periodic in the end.

The case $\mathrm{Re}=\mathbf{7{,}500}$. In Fig. 9, we display the complete phase diagram at the three relevant corners of the square cavity, the limit set being highlighted (light gray line).

The case $\mathrm{Re}=\mathbf{10{,}000}$. To start with, in Fig. 10, we display the detailed phase diagram at the top left corner, $\mathbf{x}=(\frac{1}{32},\frac{31}{32})$, the limit set being highlighted (light gray line). But here, the long-term integration is performed twice with the same time step $\Delta t=4h$. The light gray line: the initial condition is the solution of the NSE computed at the Reynolds number $\mathrm{Re}=9{,}000$. The black line: the initial condition is the solution of the Stokes equations computed at the same Reynolds number $\mathrm{Re}=10{,}000$. As time goes on, the dynamic behaviors of these two solutions of the NSE get closer and closer; the limit sets are indistinguishable. The light gray line dynamic behavior starts closer to the limit set than the black line dynamic behavior does.

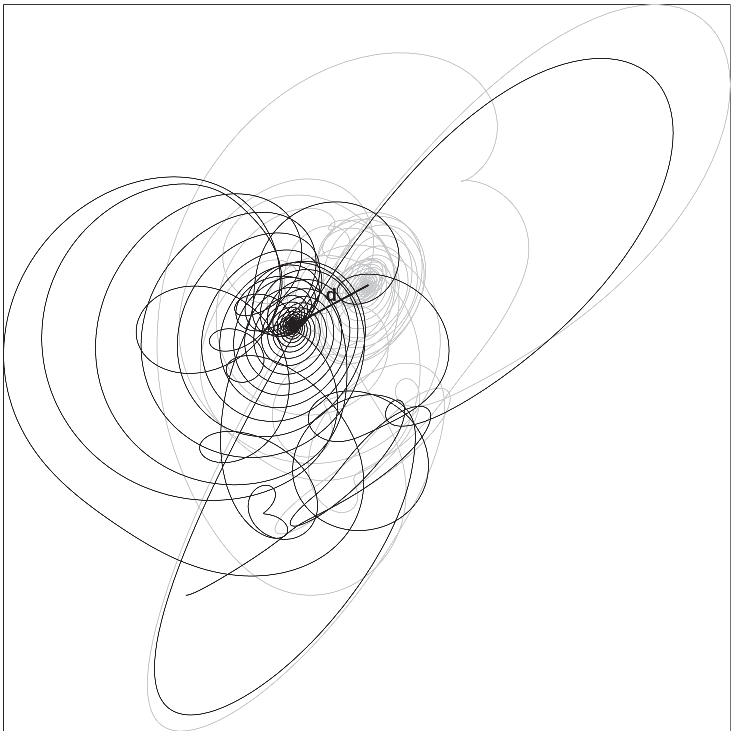

Figure 6: The complete phase diagram at the point $\mathbf{x}=(\frac{7}{8},\frac{1}{8})$. Re$=$5,000. $N=128$ (light gray line), $N=256$ (black line).

Finally, the geometrical structure of the flow and the associated physics. In Fig. 14, we display a complete cycle of streamlines for the time periodic solution.

At the bottom left corner appear two secondary vortices: DBL_2 and UBL_2. These vortices keep merging as time goes on. The primary vortex drags DBL_2 up to merge with UBL_2. When they are merging, a tertiary vortex appears; when the merging is complete, this tertiary vortex disappears. DBL_2 absorbs UBL_2 (UBL_2 disappears), and the primary vortex drags DBL_2 up to become UBL_2. Then, DBL_2 appears again. This behavior goes on periodically.

At the top left corner appear two secondary vortices: DTL_2 and UTL_2. These vortices keep merging as time goes on. The primary vortex drags DTL_2 up to merge with UTL_2. When they are merging, a tertiary vortex appears; when the merging is complete, this tertiary vortex disappears. UTL_2 absorbs DTL_2 (DTL_2 disappears), and the primary vortex drags UTL_2 up. UTL_2 never disappears. Then, DTL_2 appears again. This behavior goes on periodically. No splitting of vortices occurs at the bottom and top left corners.

At the bottom right corner, appear a secondary vortex and a tertiary vortex. Although moving periodically, these vortices remain stationary to a large extent. Neither splitting nor merging of vortices occurs at the bottom right corner.

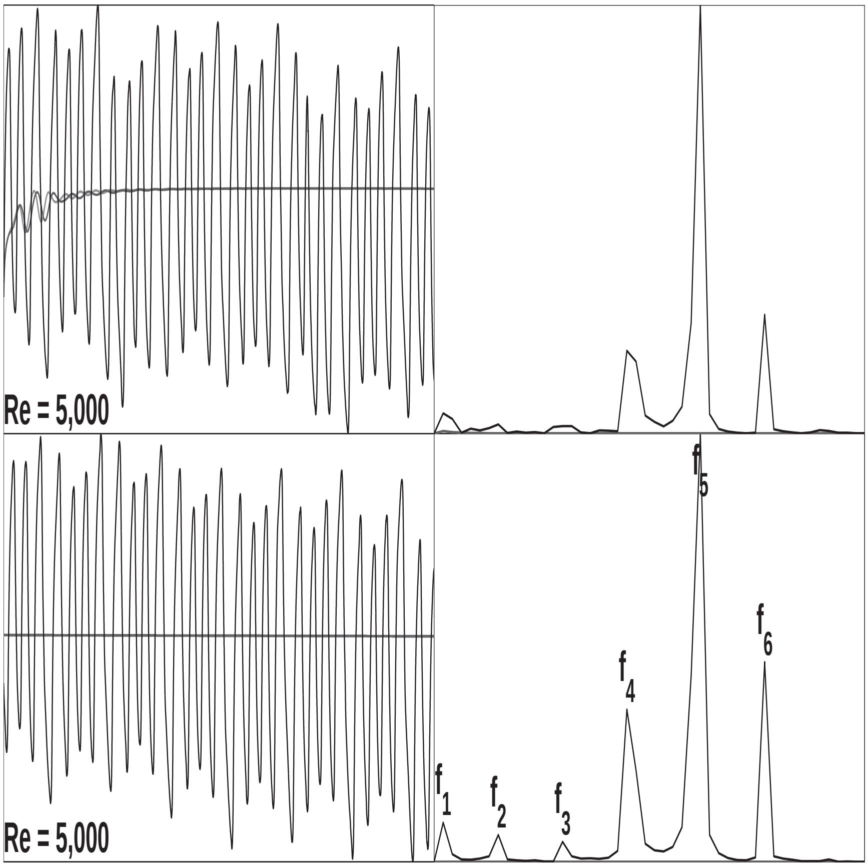

Figure 7: The time-step refinement analysis. The initial time interval (top) and the final time interval (bottom).

The case Re = **12,500.** In the first place, the time-step refinement analysis. Here, we take $\tau_1 = 4{,}375$ and $\tau_2 = 5{,}312.5$. On the initial time interval and on the final time interval with $\Delta t = 4h$, the oscillograms of the kinetic energy and the corresponding power spectra resemble. Indeed, the global attractor has been attained. This is time periodic: one fundamental frequency—$f_1 = 2.432$—the same on the initial time interval and on the final time interval sets the pace. On the initial time interval with $\Delta t = h$, $\Delta t = 2h$, and $\Delta t = 3h$, the global attractors have not yet been attained: one fundamental frequency sets the pace, but a very low frequency—with small amplitude—distances from the time periodic solution attained with $\Delta t = 4h$.

On the final interval with $\Delta t = h$, $\Delta t = 2h$, $\Delta t = 3h$, and $\Delta t = 4h$, the oscillograms of the kinetic energy and the corresponding power spectra resemble. The global attractors have been attained. These are time periodic, all. To some extent, they differ. But, they look parallel.

And, the long-term dynamic behavior at the three relevant corners of the square cavity, how do they differ? Indeed, they are time periodic, all. At the bottom right corner:

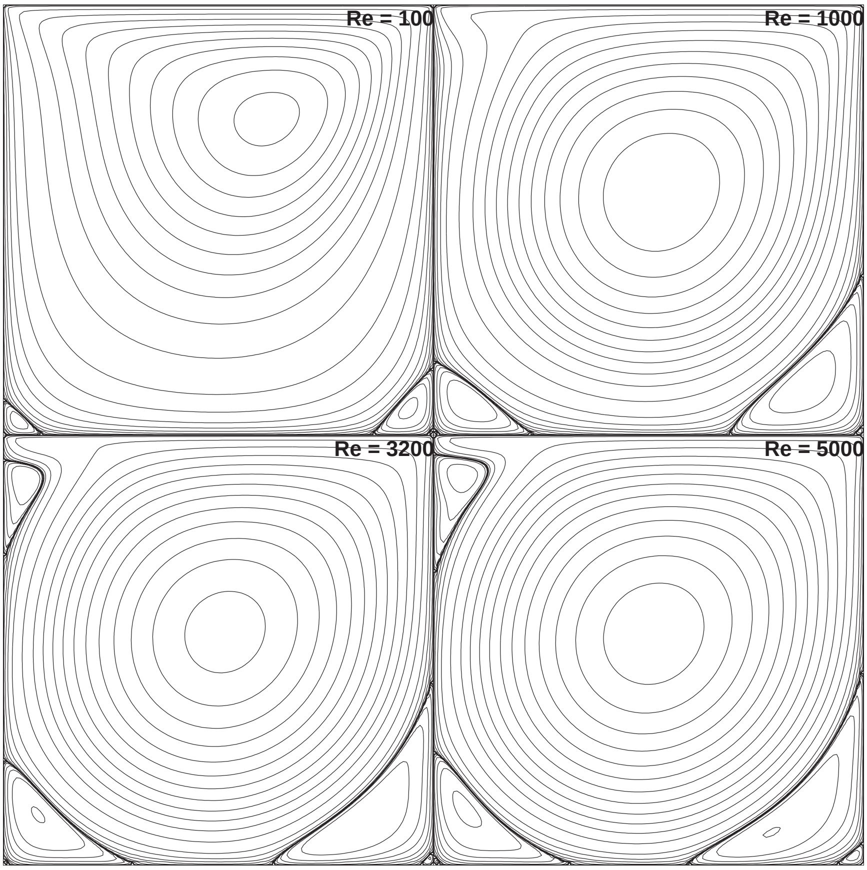

Figure 8: Low Reynolds number flow. Stationary solutions.

$\mathbf{x} = (\frac{7}{8}, \frac{1}{8})$, see Fig. 13, they are almost indistinguishable; with $\Delta t = 4h$, the fundamental frequency is $f_1 = 2.432$.

In the second place, the geometrical structure of the flow and the associated physics. In Fig. 15, we display a complete cycle of streamlines for the time periodic solution.

At the bottom and top left corners, the long-term dynamic behavior is as the one at the corresponding corners for $\mathrm{Re} = 10{,}000$.

At the bottom right corner the long-term dynamic behaviors for $\mathrm{Re} = 10{,}000$ and $\mathrm{Re} = 12{,}500$ differ. Now, at the bottom right corner appear two secondary vortices: DBR_2 and UBR_2. These vortices keep merging and splitting as time goes on. The primary vortex drags UBR_2 down to merge with DBR_2. When they are merging, two tertiary vortices and two quaternary vortices appear: DBR_3 and UBR_3, and DBR_4 and UBR_4. UBR_2 merges with the quaternary vortex DBR_4; when the merging is complete, DBR_3 disappears and UBR_3 and UBR_4 stands. UBR_2 absorbs DBR_2 (DBR_2 disappears), and the primary vortex drags UBR_2 down to become DBR_2. Then, UBR_2 appears again. Meanwhile, UBR_3 becomes stronger, and the interaction of the primary vortex and UBR_3 produces the split-

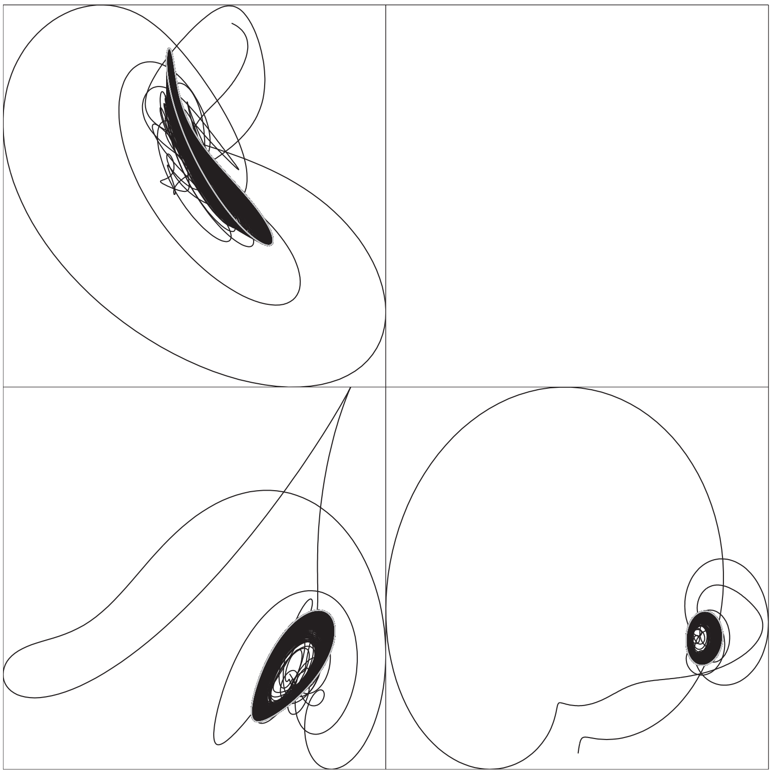

Figure 9: The long-term dynamic behavior. Re = 7,500.

ting of DBR_2 and UBR_2. Then, the tertiary vortex UBR_3 becomes weaker, and the stronger action of the primary vortex produces again the merging of DBR_2 and UBR_2. This behavior goes on periodically.

3.4 Chaotic solutions

As a matter of fact, for Re = 15,000, Re = 17,500, and Re = 20,000, the solution is neither stationary nor time periodic: the solution becomes chaotic.

The case Re = **15,000.** In the first place, the time-step refinement analysis. Here, we take $\tau_1 = 13{,}437.5$ and $\tau_2 = 14{,}375$. On the initial time interval and on the final time interval with $\Delta t = 4h$, the oscillograms of the kinetic energy and the corresponding power spectra resemble. Indeed, the global attractor has been attained. On the initial time interval, six fundamental frequencies—$f_2 =$ incipient, $f_3 = 0.4267$, $f_4 = 0.512$, $f_5 = 0.64$, $f_6 = 0.896$, $f_7 = 2.3467$—set the pace, and a very low frequency—$f_1 = 0.0853$—pushes or pulls while active; on the final time interval, six fundamental frequencies—$f_2 = 0.1707$, $f_3 = 0.384$, $f_4 = 0.5547$, $f_5 = 0.7253$, $f_6 = 0.896$, $f_7 = 2.3467$—set the pace, and a very small frequency—$f_1 = 0.0853$—pushes or pulls while active, causing chaotic behavior.

Figure 10: The long-term dynamic behavior. $\mathrm{Re}=10{,}000$.

On the initial time interval and on the final time interval with $\Delta t=h$, $\Delta t=2h$, $\Delta t=3h$, and $\Delta t=4h$, the oscillograms of the kinetic energy and the corresponding power spectra resemble. The global attractors have been attained. They are chaotic, all. To some extent, they differ. But, they look parallel.

Temporal errors do appear. And, the solutions computed later at the time τ_2, how do they differ? In Fig. 16, we display those solutions. With $\Delta t=h$, the strength of the primary vortex is -0.1161; with $\Delta t=2h$, -0.1162; with $\Delta t=3h$, -0.1160; with $\Delta t=4h$, -0.1159. The primary vortex remains stationary: its location is $(0.5117, 0.5313)$, the same with all the time steps. The small vortices appear to move clockwise: $\Delta t=h \longrightarrow \Delta t=2h \longrightarrow \Delta t=3h \longrightarrow \Delta t=4h$. The temporal errors seem to shift the time at some rate. And, the long-term dynamic behavior at the three relevant corners of the square cavity, how do they differ? Indeed, they become chaotic, all. At the bottom right corner: $\mathbf{x}=(\frac{7}{8},\frac{1}{8})$, see Fig. 13, similarly they become chaotic: with $\Delta t=4h$, one fundamental frequency—$f_1=2.3467$—sets the pace, and broadband, noise-like frequencies push or pull while active, causing chaotic behavior.

In the second place, the geometrical structure of the flow and the associated physics, see Fig. 17. Here, we take $T=14{,}382.2656$.

For the most part, at the three relevant corners of the square cavity, the long-term

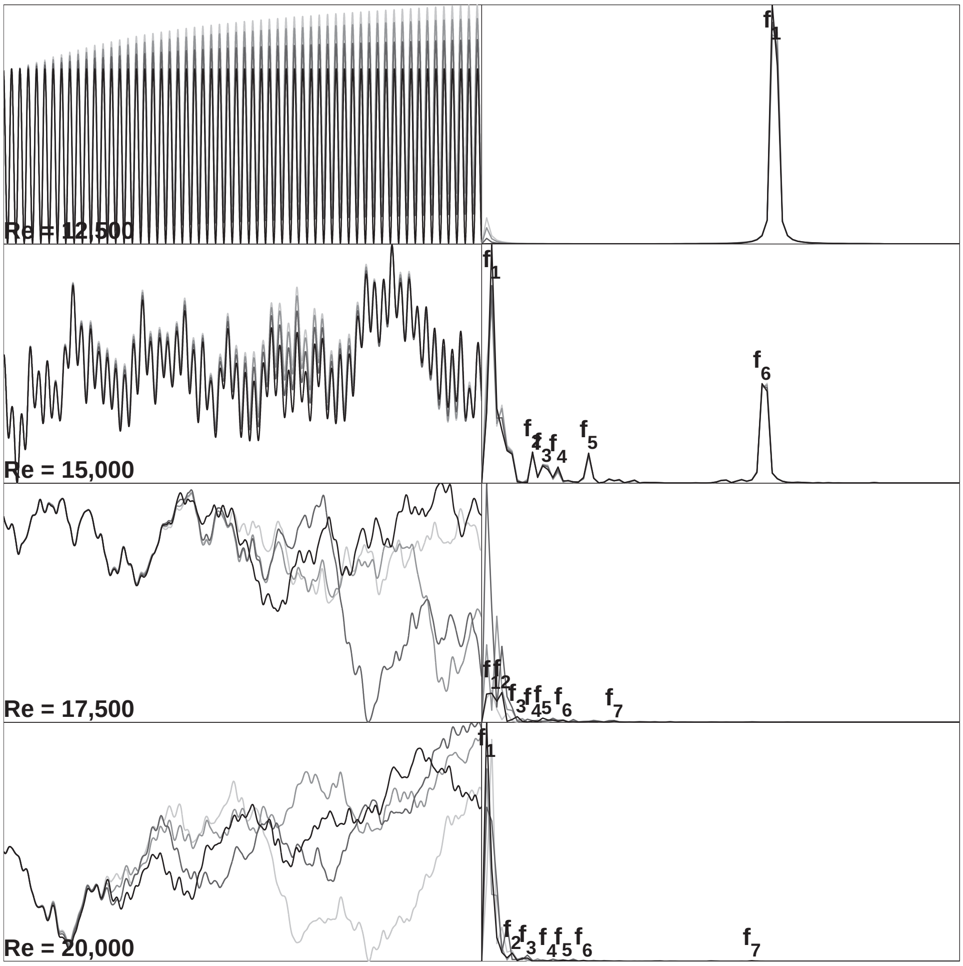

Figure 11: The time-step refinement analysis. The initial time interval.

dynamic behavior is as the one at the corresponding corners for Re = 12,500; the shape and the intensity of the vortices vary.

In addition, at the bottom left corner, sometime, the primary vortex merges with the tertiary vortex BL_3. Meanwhile, the quaternary vortex BL_4 appears fleetingly, lacking relevance. At the bottom right corner, sometime, when the two secondary vortices DBR_2 and UBR_2 are going to merge, UBR_2 merges with the quaternary vortex DBR_4, becoming stronger; the merging of UBR_2 and DBR_2 is delayed; in fact, it does not occur. Instead, two phenomena happen: first, DBR_2 becomes weaker and is dragged away to the bottom left corner to merge with DBL_2; second, UBR_2 splits by the action of the primary vortex and UBR_3, giving rise to the new DBR_2 and UBR_2. Meanwhile, the quaternary vortex UBR_4 appears fleetingly, lacking relevance.

The case Re = **17,500.** In the first place, the time-step refinement analysis. Here, we take

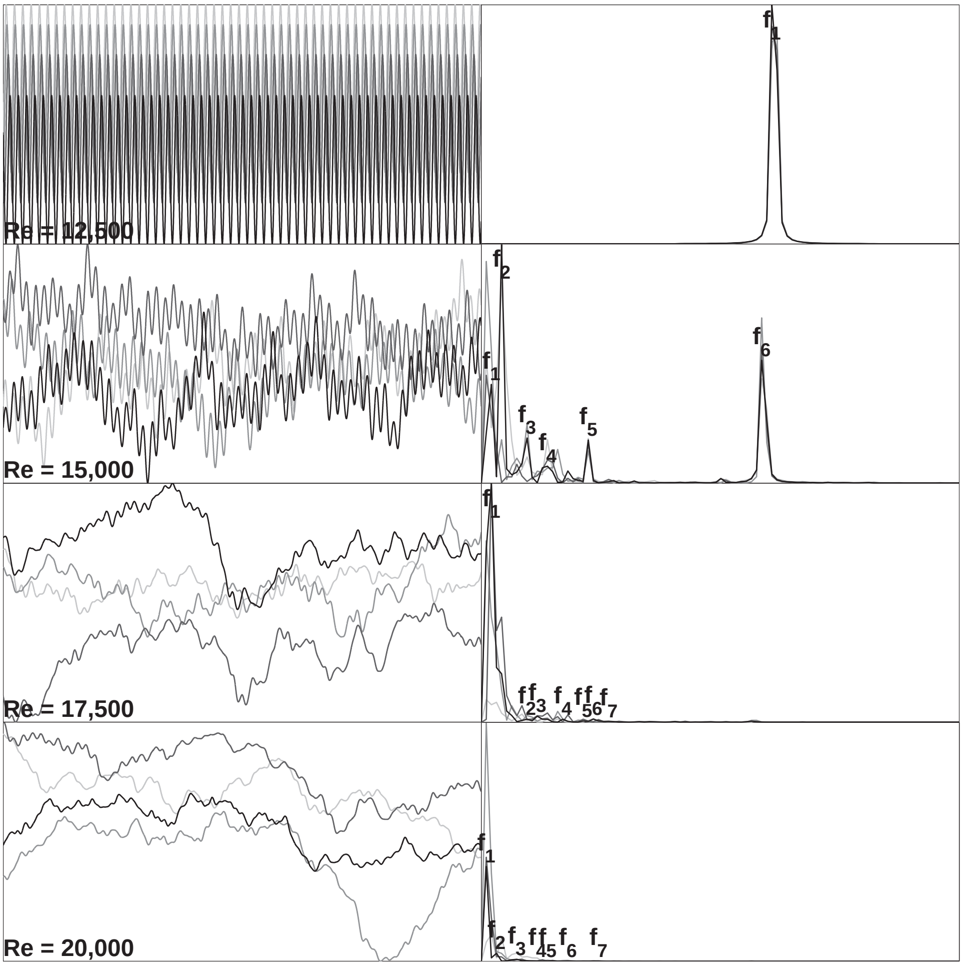

Figure 12: The time-step refinement analysis. The final time interval.

$\tau_1 = 20{,}078.125$ and $\tau_2 = 30{,}390.625$.

On the initial time interval with $\Delta t = h$, $\Delta t = 2h$, $\Delta t = 3h$, and $\Delta t = 4h$, the oscillograms of the kinetic energy coincide for a short period of time and unambiguously differ afterward. On the initial time interval and on the final time interval with $\Delta t = 4h$, the oscillograms of the kinetic energy and the corresponding power spectra differ. Indeed, on the initial time interval the global attractor has not yet been attained. Nevertheless, chaos is going on.

With $\Delta t = 4h$, on the initial time interval, six fundamental frequencies—$f_2 = 0.1707$, $f_3 = 0.2987$, $f_4 = 0.4267$, $f_5 = 0.512$, $f_6 = 0.6827$, $f_7 = 1.1093$—set the pace, and a very low frequency—$f_1 = 0.0853$—with considerable amplitude pushes or pulls while active; on the final interval, six fundamental frequencies—$f_2 = 0.3840$, $f_3 = 0.4693$, $f_4 = 0.6827$, $f_5 = 0.8533$, $f_6 = 0.9387$, $f_7 = 1.0667$—set the pace, and a very low frequency—$f_1 = 0.0853$—with large

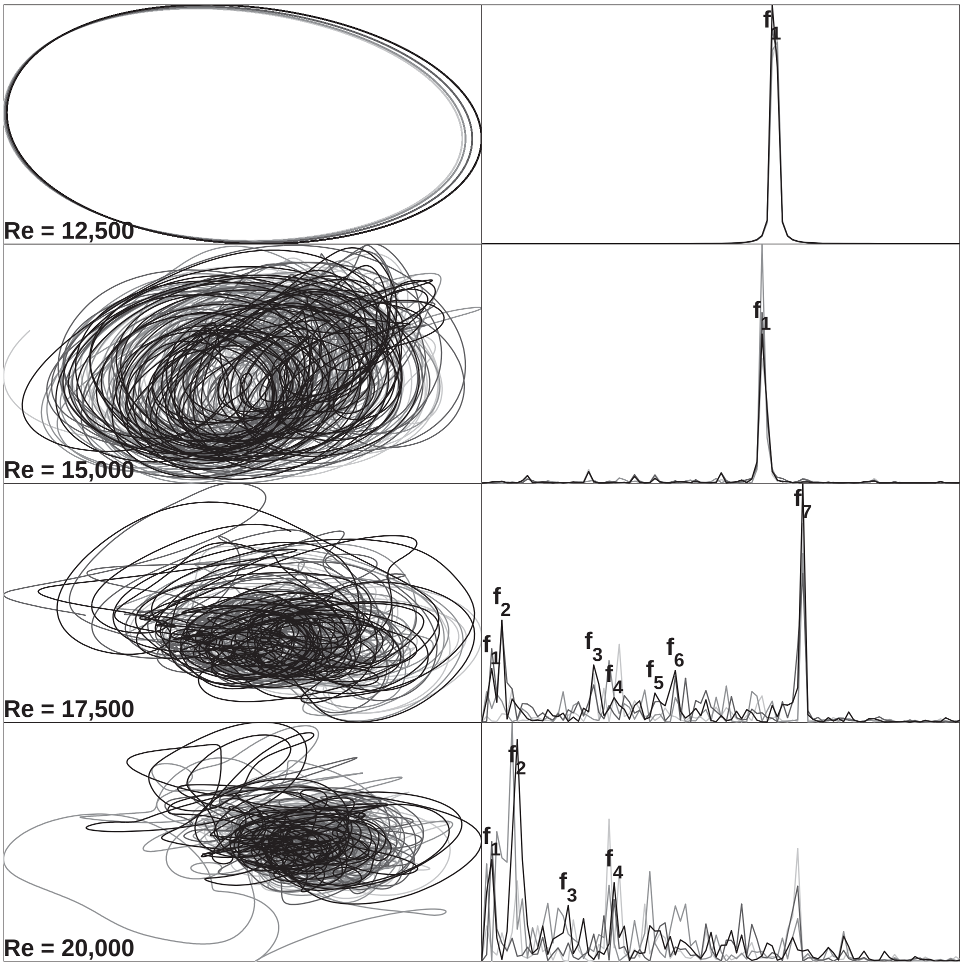

Figure 13: The phase diagram and power spectrum at the point $\mathbf{x}=(\frac{7}{8},\frac{1}{8})$. The final time interval.

amplitude pushes or pulls while active, causing chaotic behavior. But the fundamental frequencies are weak. The amplitude of f_1 on the final time interval is more than four times the amplitude of f_1 on the initial time interval. Solely two frequencies coincide on both time intervals, initial and final.

On the final time interval with $\Delta t = h$, $\Delta t = 2h$, $\Delta t = 3h$, and $\Delta t = 4h$, the oscillograms of the kinetic energy unambiguously differ throughout. They do not look parallel. The corresponding power spectra resemble: a very low frequency dominates the spectra over weak fundamental frequencies. The global attractor has not been attained neither on the final time interval.

And, the long-term dynamic behavior at the three relevant corners of the square cavity, how do they differ? Indeed, they become chaotic, all. At the bottom right corner: $\mathbf{x} = (\frac{7}{8},\frac{1}{8})$, see Fig. 13, similarly they go chaotic: with $\Delta t = 4h$, six fundamental

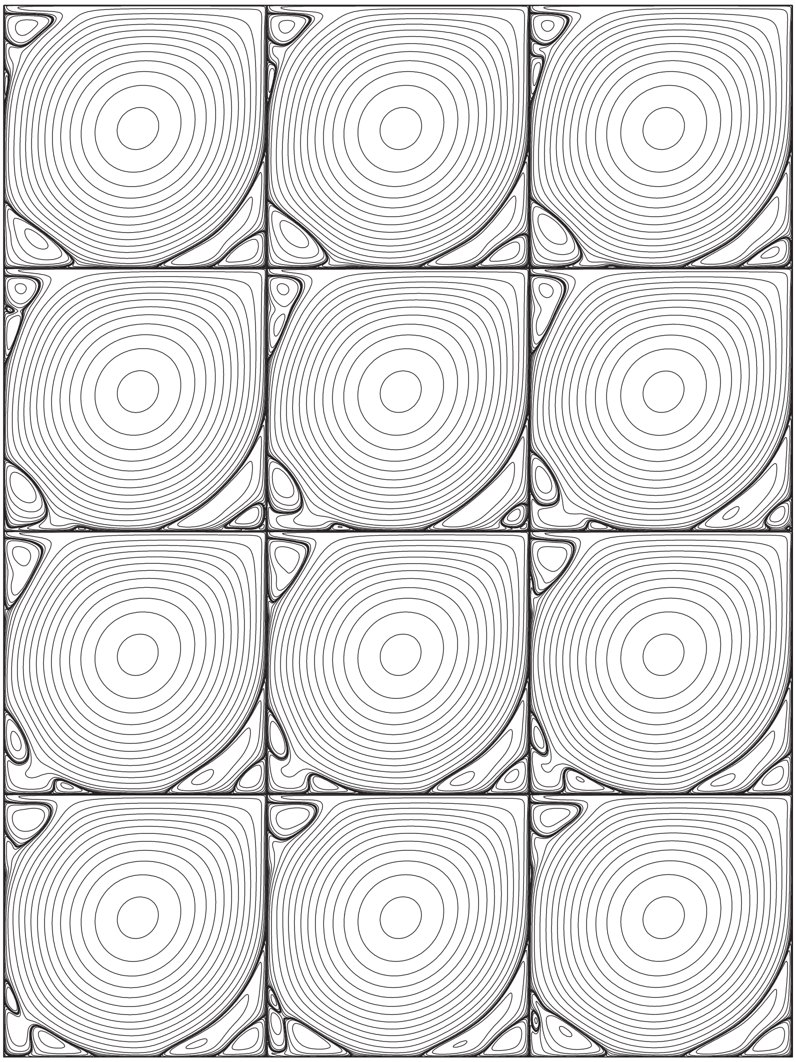

Figure 14: A complete cycle of streamlines. $\mathrm{Re}=10{,}000$.

frequencies—$f_2=0.1707$, $f_3=0.9387$, $f_4=1.1093$, $f_5=1.4507$, $f_6=1.6213$, $f_7=2.688$—set the pace, and a very low frequency—$f_1=0.0853$—and broadband, noise-like frequencies push or pull while active, causing chaotic behavior. Now, the very low frequency is weaker than the fundamental frequencies. This seems an indication that the global attractor has been attained at the bottom right corner.

In the second place, the geometrical structure of the flow and the associated physics, see Fig. 18. Here, we take $T=21{,}021.7969$.

For the most part, at the three relevant corners of the square cavity, the long-term dynamic behavior is as the one at the corresponding corners for $\mathrm{Re}=15{,}000$; the shape and the intensity of the vortices vary.

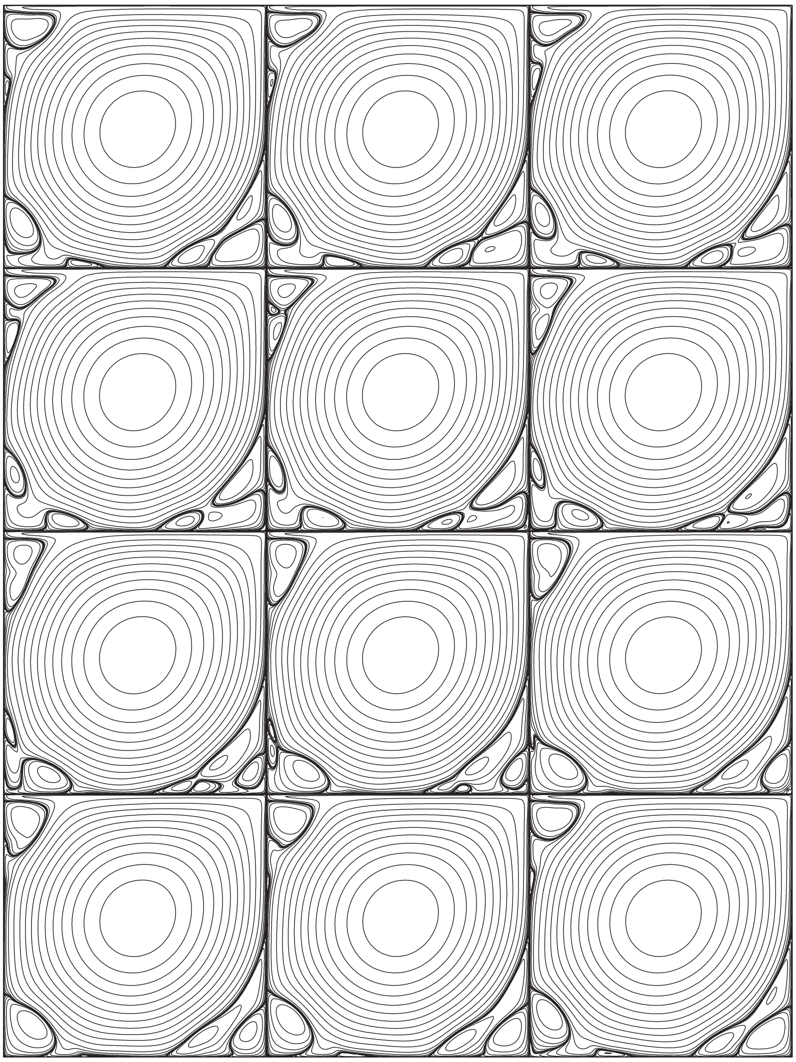

Figure 15: A complete cycle of streamlines. Re = 12,500.

Furthermore, at the bottom right corner, sometime, when the two secondary vortices DBR_2 and UBR_2 are going to merge, the merging is delayed; in fact, it does not occur. Instead, two phenomena happen: first, DBR_2 becomes weaker and is dragged away to the bottom left corner to merge with DBL_2; second, the interaction of the primary vortex and UBR_3 splits UBR_2, giving rise to the new DBR_2 and UBR_2. Then, DBR_2 and UBR_2 go to merge again. When they are about to merge, DBR_3 arises, and the interaction of DBR_3 and UBR_3 splits DBR_2, giving rise to the new DBR_2 and BR_4. DBR_3 and UBR_3 merge, and DBR_2 and UBR_2 merge. Meanwhile, the quaternary vortex BR_4 stands.

The case Re = **20,000.** In the first place, the time-step refinement analysis. Here, we take

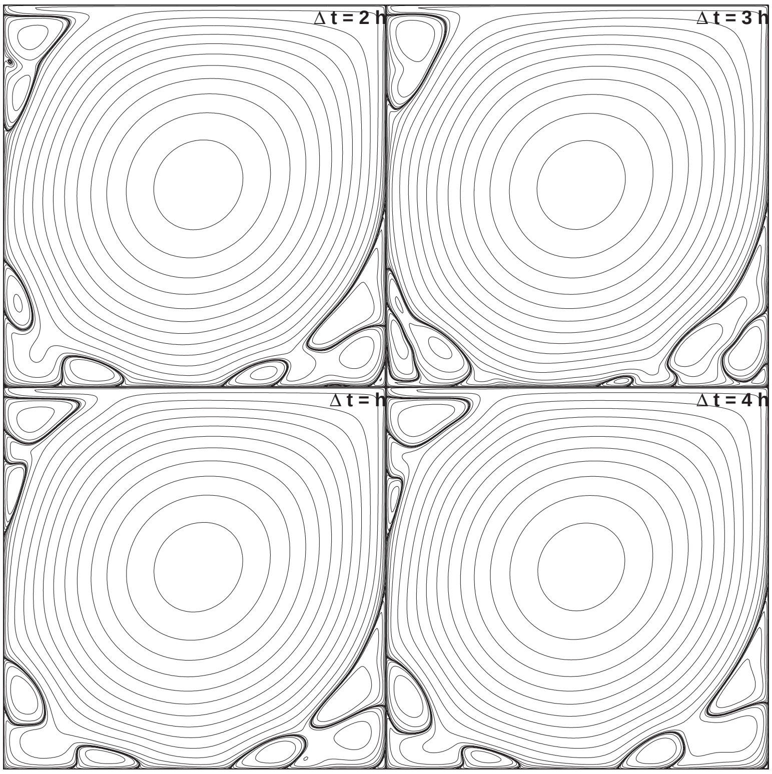

Figure 16: The effect of temporal errors. $\mathrm{Re}=15{,}000$.

$\tau_1=25{,}312.5$ and $\tau_2=26{,}250$.

On the initial time interval with $\Delta t{=}h$, $\Delta t{=}2h$, $\Delta t{=}3h$, and $\Delta t{=}4h$, the oscillograms of the kinetic energy coincide for a shorter period of time than in the case before $\mathrm{Re}=17{,}500$ and unambiguously differ afterward. On the initial time interval and on the final interval with $\Delta t=4h$, the oscillograms of the kinetic energy and the corresponding power spectra differ. Indeed, on the initial time interval the global attractor has not yet been attained. Nevertheless, chaos is going on.

With $\Delta t=4h$, on the initial time interval, six fundamental frequencies—$f_2=0.256$, $f_3=0.384$, $f_4=0.5547$, $f_5=0.6827$, $f_6=0.8533$, $f_7=2.2613$—set the pace, and a very low frequency—$f_1=0.0427$—with large amplitude pushes or pulls while active, causing chaotic behavior; on the final time interval, six fundamental frequencies—$f_2=0.128$, $f_3=0.2987$, $f_4=0.4693$, $f_5=0.5547$, $f_6=0.7253$, $f_7=0.9813$—set the pace, and a very low frequency—$f_1=0.0427$—with large amplitude pushes or pulls while active, causing chaotic behavior. But the fundamental frequencies are weak, the very low frequency having extremely large amplitude, and differ on both time intervals, initial and final, for the most part.

On the final time interval with $\Delta t=h$, $\Delta t=2h$, $\Delta t=3h$, and $\Delta t=4h$, the oscillograms of the kinetic energy unambiguously differ throughout. They do not look parallel. The

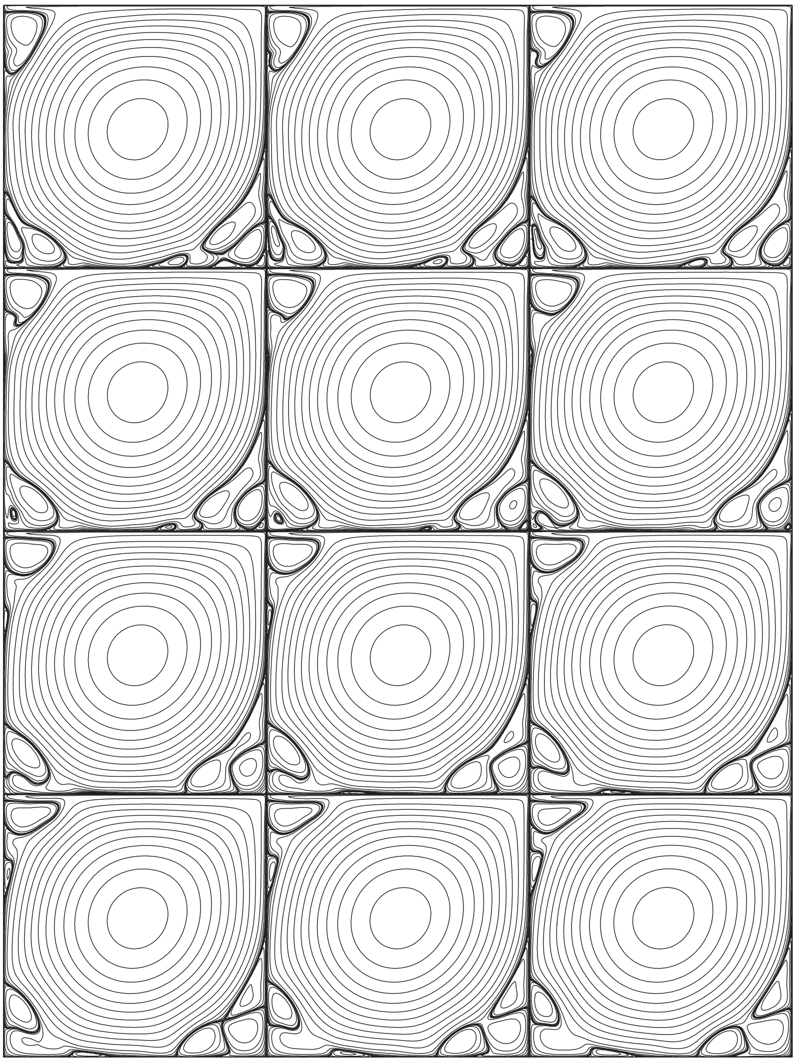

Figure 17: A partial sequence of streamlines. Re = 15,000.

global attractors have not been attained either on the final interval.

And the long-term dynamic behavior at the three relevant corners of the square cavity, how do they differ? Indeed, they become chaotic, all. At the bottom right corner: $\mathbf{x} = (\frac{7}{8}, \frac{1}{8})$, see Fig. 13, similarly they become chaotic: with $\Delta t = 4h$, three fundamental frequencies—f_2=0.2987, f_3=0.7253, f_4=1.1093—set the pace, and a very low frequency—$f_1 = 0.0853$—and broadband, noise-like frequencies push or pull while active, causing chaotic behavior. Now, the very low frequency is weaker than the not clear-cut, but arising fundamental frequencies. This seems an indication that the global attractor has not yet been attained at the bottom right corner.

The global attractor has not yet been attained although the time reached is extremely

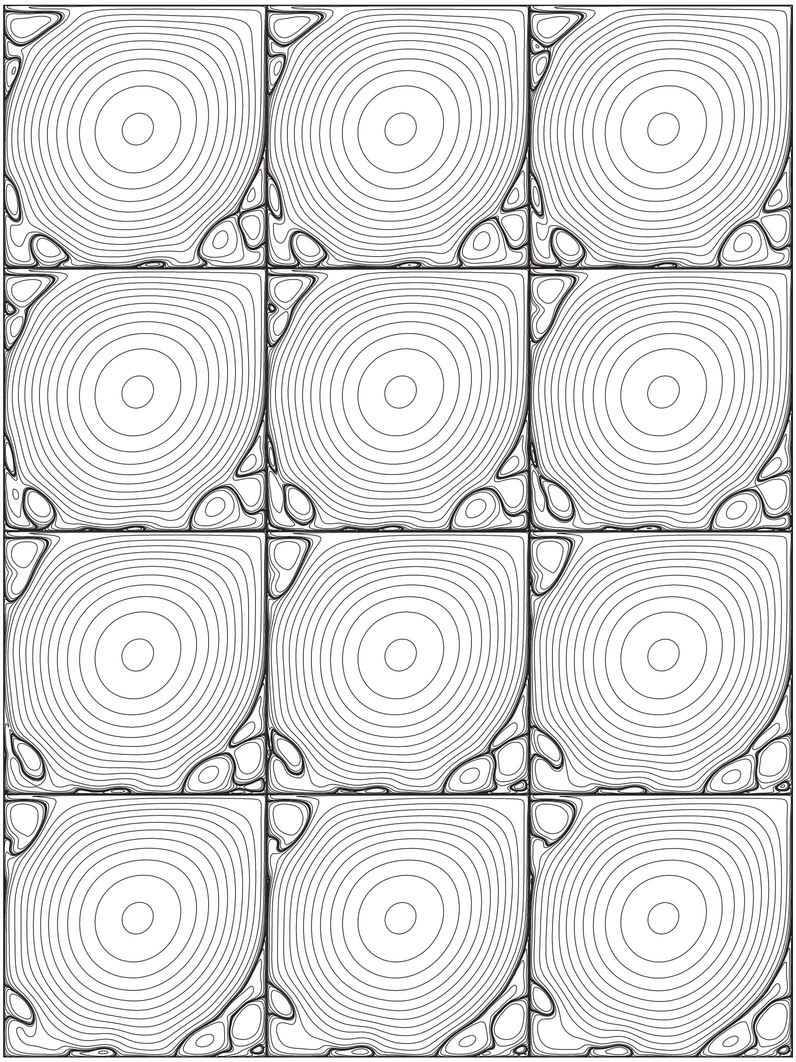

Figure 18: A partial sequence of streamlines. $\mathrm{Re}=17{,}500$.

large and the initial condition is the last computed solution of the NSE at the Reynolds number considered just before $\mathrm{Re}=17{,}500$—the very low frequency having extremely large amplitude, not allowing to perceive the fundamental frequencies, for the most part.

Finally, the small vortices in the flow decay exponentially toward a small value; e.g., the displayed plane segment in Fig. 13 bottom left is $[-0.2547,0.2773]\times[-0.1504,0.3036]$.

In the second place, the geometrical structure of the flow and the associated physics, see Fig. 19. Here, we take $T=26{,}253.5938$.

To some extent, at the three relevant corners of the square cavity, the long-term dynamic behavior is as the one at the corresponding corners for $\mathrm{Re}=17{,}500$; the shape and the intensity of the vortices vary.

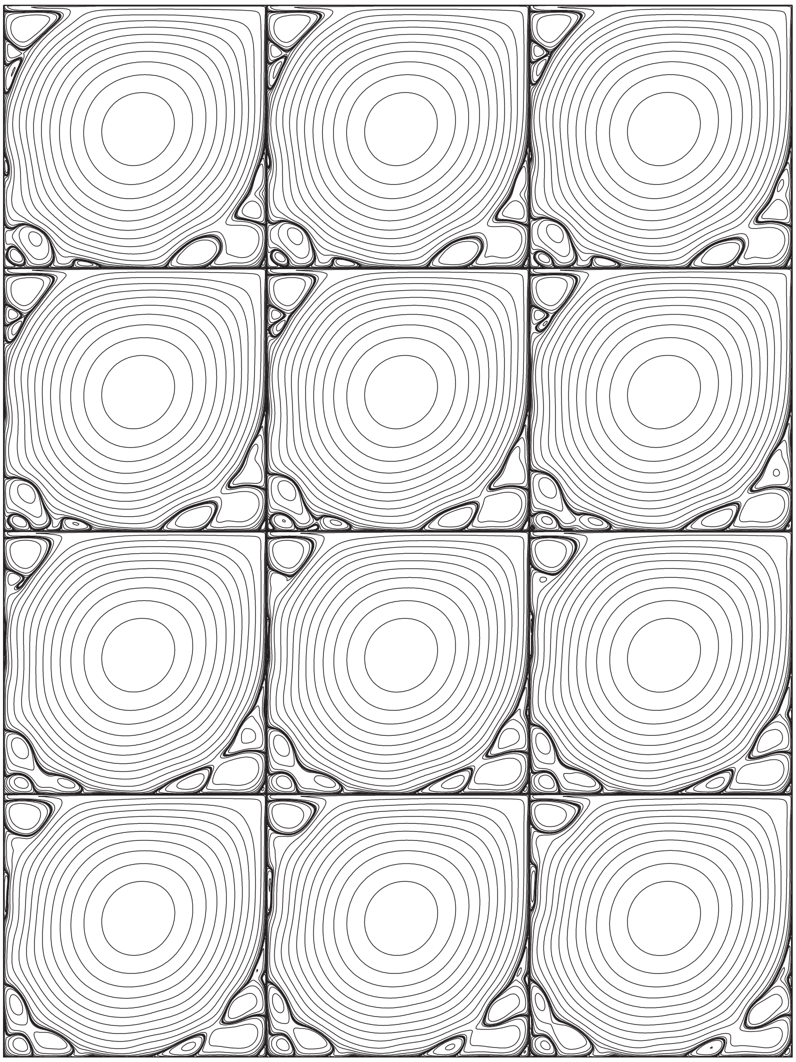

Figure 19: A partial sequence of streamlines. Re = 20,000.

Furthermore, at the top left corner, sometime, the tertiary vortex TL_3 is so strong that it does not disappear and it impedes the merging of DTL_2 and UTL_2; instead, DTL_2 is dragged up, and almost simultaneously, TL_3 and DTL_2 disappear. At the bottom left corner the interaction of the vortices down UBL_2 is such that any merging with UBL_2 is delayed; in fact, it does not occur. Instead, UBL_2 becomes weaker and is dragged up to the top left corner to merge with DTL_2.

3.5 Quantitative and qualitative comparisons

Let us now make some detailed comparisons of quantities.

Table 2: The bottom right secondary vortex.

	Re = 1,000		Re = 5,000	
Authors	strength	location	strength	location
Present	1.79×10^{-3}	(0.8594,0.1094)	3.07×10^{-3}	(0.7891,0.0781)
Erturk et al.	1.73×10^{-3}	(0.8633,0.1117)	3.06×10^{-3}	(0.8050,0.0733)
Barragy and Carey	—	—	3.07×10^{-3}	(0.8041,0.0725)
Goyon	1.63×10^{-3}	(0.8671,0.1171)	2.82×10^{-3}	(0.8203,0.0781)
Vanka	1.74×10^{-3}	(0.8625,0.1063)	5.49×10^{-3}	(0.8500,0.0813)
Schreiber and Keller	1.70×10^{-3}	(0.8643,0.1071)	—	—
Ghia et al.	1.75×10^{-3}	(0.8594,0.1094)	3.08×10^{-3}	(0.8086,0.0742)

In the first place, in Table 2 we highlight the characteristics of BR_2 for Re = 1,000 and Re=5,000. First, the quantities we obtained with N=128 and Δt=4h are displayed. Then, the quantities obtained by the other authors are displayed chronologically. For Re=1,000, our results agree with those obtained by all authors except [21]. The results obtained in [21] disagree with those obtained by the other authors: the strength of BR_2 is weaker, for the most part. For Re = 5,000, our results agree with those obtained in [1,10], and [19] and differ with those obtained in [21] and [35]. The results obtained in [21] and [35] disagree with those obtained by the other authors: according to [21], the strength of BR_2 is weaker; according to [35], stronger, for the most part.

In the second place, in Tables 3 and 4 we highlight the characteristics of the primary vortex for Re = 5,000, Re = 7,500, Re = 10,000, and Re = 12,500. First, the quantities we obtained with N=256 and Δt=4h are displayed. Then, when available, the quantities obtained by the other authors are displayed chronologically. For these Reynolds numbers, our results agree with those obtained in [1,10], and [23] and disagree with those obtained in [19] where the strength of the primary vortex is systematically weakened. The results obtained in [21,35], and [26] differ significantly from those obtained by the other authors, the strength of the primary vortex being substantially weaker.

On the other hand, [1,10,23,26,35], and [19] consider the stationary NSE, but in [21] and in the present research, the time-dependent NSE; so that qualitative comparisons are possible with [21].

In [21] the author reports stationary solutions in a row from Re = 100 to Re = 7,500—and time periodic solutions in a row for Re = 10,000 and Re = 12,500. Notwithstanding, we report stationary solutions in a row from Re = 100 to Re = 5,000—and time periodic solutions in a row from Re = 7,500 to Re = 12,500, this kind of solutions occurring for smaller Reynolds numbers in the present research. Furthermore, the long-term dynamic behavior we observed for Re=10,000 has been reported in [21]—but for a larger Reynolds number: Re = 12,500, where, besides, the merging and splitting of secondary vortices at the bottom right corner is incipient, ibid., p. 332.

Finally, the mesh-size refinement analysis, see Table 5. Here, we highlight the char-

Table 3: The primary vortex.

	Re = 5,000		Re = 7,500	
Authors	strength	location	strength	location
Present	−0.1237	(0.5156,0.5352)	−0.1246	(0.5117,0.5313)
Erturk et al.	−0.1213	(0.5150,0.5350)	−0.1209	(0.5133,0.5317)
Barragy and Carey	−0.1222	(0.5151,0.5359)	−0.1224	(0.5132,0.5321)
Goyon	−0.1115	(0.5156,0.5391)	−0.1052	(0.5156,0.5312)
Li et al.	−0.1204	(0.5156,0.5391)	−0.1194	(0.5156,0.5391)
Vanka	−0.0920	(0.5125,0.5313)	—	—
Schreiber and Keller	—	—	—	—
Ghia et al.	−0.1190	(0.5117,0.5352)	−0.1200	(0.5117,0.5322)

Table 4: The primary vortex (continued).

	Re = 10,000		Re = 12,500	
Authors	strength	location	strength	location
Present	−0.1230	(0.5117,0.5313)	−0.1199	(0.5117,0.5313)
Erturk et al.	−0.1204	(0.5117,0.5300)	−0.1198	(0.5117,0.5283)
Barragy and Carey	−0.1224	(0.5113,0.5302)	−0.1224	(0.5113,0.5283)
Goyon	—	—	—	—
Vanka	—	—	—	—
Schreiber and Keller	−0.1028	(0.5140,0.5307)	—	—
Ghia et al.	−0.1197	(0.5117,0.5333)	—	—

Table 5: Characteristics of the vortices. Re = 5,000.

	$n=128$		$n=256$	
Vortices	strength	location	strength	location
Primary	−0.1270	(0.5156,0.5391)	−0.1237	(0.5156,0.5352)
BL_2	0.0012	(0.0703,0.1328)	0.0014	(0.0742,0.1328)
BR_2	0.0031	(0.7891,0.0781)	0.0031	(0.8008,0.0742)
TL_2	0.0016	(0.0625,0.9063)	0.0015	(0.0625,0.9102)
BL_3	-1.61×10^{-7}	(0.0078,0.0078)	-1.21×10^{-7}	(0.0078,0.0078)
BR_3	-1.93×10^{-6}	(0.9766,0.0234)	-1.67×10^{-6}	(0.9766,0.0195)

acteristics of the vortices for Re = 5,000. The quantities obtained in the present research with $N=128$ and $\Delta t=4h$, and $N=256$ and $\Delta t=4h$ are compared. For the primary vortex, the difference between the strengths is -3.29×10^{-3}; for BL_2, -1.35×10^{-4}; for BR_2, -1.33×10^{-5}; for TL_2, 5.47×10^{-5}; for BL_3, -3.97×10^{-8}; for BR_3, -2.61×10^{-7}. Furthermore, all the corresponding x- and y-directions components of the locations of the vortices considered, exactly a half of them differ. For the primary vortex and BL_2 and

TL_2 and BR_3, the distance between the locations is 3.91×10^{-3}; for BR_2, 1.24×10^{-2}; for BL_3, 0—no disagreements are there.

The computations were carried out in double precision arithmetic on the Silicon Graphics Octane. From Netlib, blas, lapack, bihar, fftpack, and vfftpack were used to do the numerical codes. Matlab was used to do the graphics and to fill out the tables.

4 Conclusion

Beginning at Re=7,500, at the bottom and top left corners, appear two secondary vortices that keep merging as time goes on. Beginning at Re = 12,500, at the bottom right corner, appear two secondary vortices that keep merging and splitting as time goes on. Beginning at Re = 15,000, the interaction of all the vortices—primary, secondary, tertiary, and quaternary—is such that small secondary vortices may be dragged away from the bottom right corner to the bottom left corner and from the bottom left corner to the top left corner. Beginning at Re = 20,000, at the top left corner, sometime, the tertiary vortex becomes so strong that it does not disappear and it impedes the merging of the secondary vortices; instead, the secondary vortex on the bottom of the top left corner is dragged up to disappear almost simultaneously with the tertiary vortex. The primary vortex stays put. The long-term dynamic behavior of the small vortices is stationary, for low Reynolds numbers; time periodic, for moderate Reynolds numbers; chaotic, for high Reynolds numbers; this behavior determines the nature of the solutions. For high Reynolds numbers, over weak fundamental frequencies appears a very low frequency dominating the spectra—this very low frequency being weaker than clear-cut fundamental frequencies seems an indication that the global attractor has been attained. The global attractor seems reached for Reynolds numbers up to Re = 15,000.

Acknowledgments

The author thanks Prof. Edriss S. Titi and the Department of Mathematics, University of California, Irvine, USA, for giving him the supercomputing support that allowed this research to be done.

The author thanks Prof. Roger Temam for inviting him to visit the Institute for Scientific Computing and Applied Mathematics, Indiana University, Bloomington, IN, USA, where the research reported herein was finalized.

This research was supported in part by the National Science Foundation Grant No. DMS-0604235.

References

[1] E. Barragy and G. F. Carey, Stream function-vorticity driven cavity solution using p finite elements, Comput. Fluids, 26(5) (1997), 453–468.

[2] M. Chen, A. Miranville and R. Temam, Incremental unknowns in finite differences in three space dimensions, Comp. Appl. Math., 14(3) (1995), 219–252.
[3] M. Chen and R. Temam, The incremental unknown method I, Appl. Math. Lett., 4(3) (1991), 73–76.
[4] M. Chen and R. Temam, The incremental unknown method II, Appl. Math. Lett., 4(3) (1991), 77–80.
[5] M. Chen and R. Temam, Incremental unknowns for solving partial differential equations, Numer. Math., 59(3) (1991), 255–271.
[6] M. Chen and R. Temam, Incremental unknowns for convection-diffusion equations, Appl. Numer. Math., 11 (1993), 365–383.
[7] M. Chen and R. Temam, Incremental unknowns in finite differences: Condition number of the matrix, SIAM J. Matrix Anal. Appl., 14(2) (1993), 432–455.
[8] M. Chen and R. Temam, Nonlinear Galerkin method in the finite difference case and wavelet-like incremental unknowns, Numer. Math., 64(3) (1993), 271–294.
[9] P. Concus, G. H. Golub and D. P. O'Leary, A generalized conjugate gradient method for the numerical solution of elliptic partial differential equations, in: J. R. Bunch and D. J. Rose (Eds.), Sparse Matrix Computations, Academic Press, 1976, pp. 309–332.
[10] E. Erturk, T. C. Corke and C. Gokcol, Numerical solutions of 2-D steady incompressible driven cavity flow at high Reynolds numbers, Int. J. Numer. Meth. Fluids, 48(7) (2005), 747–774.
[11] C. Foias, O. Manley and R. Temam, Modelling of the interaction of small and large eddies in two dimensional turbulent flows, RAIRO Modél. Math. Anal. Numér., 22(1) (1998), 93–114.
[12] S. Garcia, The matricial framework for the incremental unknowns method, Numer. Func. Anal. Opt., 14(1 & 2) (1993), 25–44.
[13] S. Garcia, Numerical study of the incremental unknowns method, Numer. Meth. Part. Diff. Eq., 10(1) (1994), 103–127.
[14] S. Garcia, Higher-order incremental unknowns, hierarchical basis, and nonlinear dissipative evolutionary equations, Appl. Numer. Math., 19(4) (1996), 467–494.
[15] S. Garcia, Algebraic conditioning analysis of the incremental unknowns preconditioner, Appl. Math. Model., 22(4–5) (1998), 351–366.
[16] S. Garcia, Incremental unknowns for solving the incompressible Navier-Stokes equations, Math. Comput. Simulat., 52(5-6) (2000), 445–489.
[17] S. Garcia, Incremental unknowns and graph techniques in three space dimensions, Appl. Numer. Math., 44(3) (2003), 329–365.
[18] S. Garcia and F. Tone, Incremental unknowns and graph techniques with in-depth refinement, Int. J. Numer. Anal. Model., 4(2) (2007), 143–177.
[19] U. Ghia, K. N. Ghia and C. T. Shin, High-Re solutions for incompressible flow using the Navier-Stokes equations and a multigrid method, J. Comput. Phys., 48(3) (1982), 387–411.
[20] R. Glowinski, Finite Element Methods for the Numerical Simulation of Incompressible Viscous Flow. Introduction to the Control of the Navier-Stokes Equations, Lectures in Applied Mathematics, Vol. 28, American Mathematical Society, 1991.
[21] O. Goyon, High-Reynolds number solutions of Navier-Stokes equations using incremental unknowns, Comput. Meth. Appl. Mech. Engrg., 130(3–4) (1996), 319–335.
[22] F. H. Harlow and J. E. Welch, Numerical calculation of time-dependent viscous incompressible flow of fluid with free surface, Phys. Fluids, 8(12) (1965), 2182–2189.
[23] M. Li, T. Tang and B. Fornberg, A compact fourth-order finite difference scheme for the steady incompressible Navier-Stokes equations, Int. J. Numer. Meth. Fluids, 20(10) (1995),

1137–1151, 1995.

[24] P. Poullet, Staggered incremental unknowns for solving Stokes and generalized Stokes problems, Appl. Numer. Math., 35(1) (2000), 23–41.

[25] V. Sarin and A. Sameh, An efficient iterative method for the generalized Stokes problem, SIAM J. Sci. Comput., 19(1) (1998), 206–226.

[26] R. Schreiber and H. B. Keller, Driven cavity flows by efficient numerical techniques, J. Comput. Phys., 49 (1983), 310–333.

[27] P. N. Shankar and M. D. Deshpande, Fluid mechanics in the driven cavity, Annu. Rev. Fluid Mech., 32 (2000), 93–136.

[28] A. Smith and D. Silvester, Implicit algorithms and their linearisation for the transient incompressible Navier-Stokes equations, IMA J. Numer. Anal., 17(4) (1997), 527–545.

[29] P. N. Swarztrauber, The methods of cyclic reduction, Fourier analysis and the FACR algorithm for the discrete solution of Poisson's equation on a rectangle, SIAM Rev., 19(3) (1977), 490–501.

[30] R. A. Sweet, Direct methods for the solution of Poisson's equation on a staggered grid, J. Comput. Phys., 12(3) (1973), 422–428.

[31] R. Temam, Inertial manifolds and multigrid methods, SIAM J. Math. Anal., 21(1) (1990), 154–178.

[32] R. Temam, Infinite Dimensional Dynamical Systems in Mechanics and Physics, Applied Mathematical Sciences, No. 68, Springer-Verlag, 1997.

[33] R. Temam, Navier-Stokes Equations: Theory and Numerical Analysis, AMS Chelsea Publishing, American Mathematical Society, 2001.

[34] H. A. van der Vorst, Bi-CGSTAB: A fast and smoothly converging variant of Bi-CG for the solution of nonsymmetric linear systems, SIAM J. Sci. Statist. Comput., 13(2) (1992), 631–644.

[35] S. P. Vanka, Block-implicit multigrid solution of Navier-Stokes equations in primitive variables, J. Comput. Phys., 65 (1986), 138–158.